Characterisation of uranium-pyrite associations within organic-rich Eocene sediments using EM, XFM-μXANES and μXRD

Susan A Cumberland[1,2,3], Katy Evans[4], Grant Douglas[5], Martin de Jonge[2], Louise Fisher[6], Daryl Howard[2], John W Moreau[1,7]

1 School of Earth Sciences, The University of Melbourne, Parkville 3010, Melbourne, Victoria, Australia
2 ANSTO-Australian Synchrotron, 800 Blackburn Road, Clayton 3163, Melbourne, Victoria, Australia
3 Current Address: University of Strathclyde, Dept. of Civil and Environmental Engineering, Glasgow, Scotland, UK
4 Curtin University, Bentley, Western Australia, Australia
5 CSIRO Land and Water, Wembley, Western Australia, Australia
6 Australia CSIRO Mineral Resources, Bentley, Western Australia, Australia
7 School of Geographical and Earth Sciences, University of Glasgow, Scotland, UK

Abstract

Sediments that are rich in organic matter (OM) can trap and accumulate metals, including uranium (U), and provide favourable conditions for the formation of minerals such as pyrite. In OM-sediments, pyrite may play an important role in sorption and reduction of U and other metals that are sensitive to redox change. Mulga Rock, located in Western Australia, is an Eocene polymetallic deposit hosting economic uranium within its OM-rich sediments. Our previous work on the Mulga Rock deposits showed that OM may host U(VI) for long periods and suggested that reduction to U(IV) may occur through different pathways. Framboidal-like pyrite, embedded in lignite, displaying U(IV)-rich rims, > 100 μm, were investigated using synchrotron-X-ray fluorescence microscopy-micro-X-ray absorption near edge structure (XFM-μXANES), laboratory micro-X-ray diffraction (μXRD) and electron microscopy. Micro-XRD analyses indicated that the U(IV) phase was mostly coffinite [$USiO_4$] mixed with uraninite [UO_2]. Analyses of transects across U-pyrite rims using XFM and XFM-μXANES revealed higher concentrations of U(IV) near the pyrite, and proportionally more U(VI) away from the edge of the pyrite. We infer that within OM environments, pyrite has a local influence on the oxidation state of U, which may be influential when considering U mobility.

Keywords: Uranium, pyrite, oxidation state, synchrotron, organic sediments, Mulga Rock

Graphical Abstract

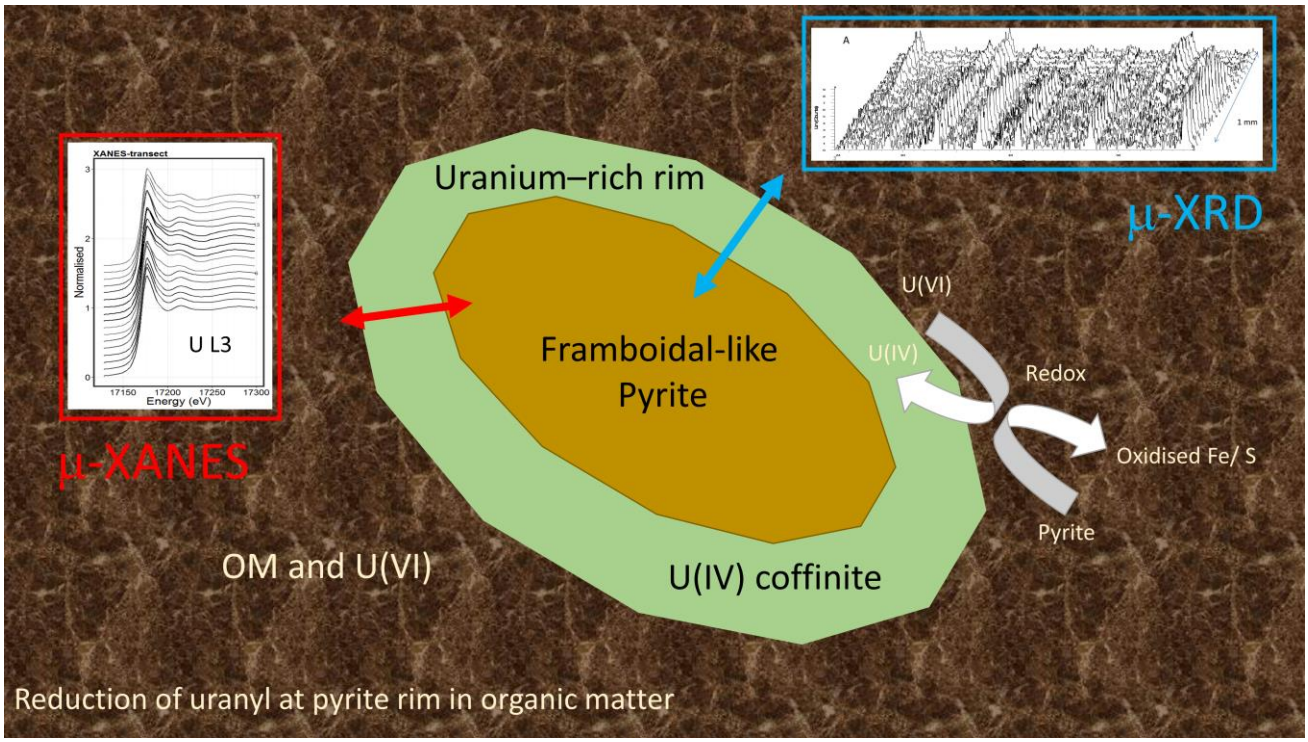

2

Highlights

- Uranium-rich rims are associated with pyrite grains in organic sediments.
- The U-layer is 100s of microns thick.
- The U at the pyrite edge consists of a mix of U(IV), coffinite and uraninite.
- The proportion of U(VI) increases with distance from pyrite.
- Organic matter-hosted pyrite may be important for U immobilisation.

3

1 Introduction

1.1 Uranium and organic matter

Sediments rich in organic matter (OM) can accumulate uranium (U), and other metals, from groundwater and hydrothermal fluids (Greenwood et al., 2012) and over time may reach economic concentrations. Examples of OM-U-rich sediments are found in the Grants Region, Texas (Deditius et al., 2008; Hansley and Spirakis, 1992) and the Mulga Rock, polymetallic deposits, Western Australia (Cumberland et al., 2018a; Douglas et al., 2011; Jaraula et al., 2015).

The mobility and deposition of U are largely determined by two main oxidation states (U(IV) and U(VI)), pH, Eh, and complexation with ligands (Langmuir, 1978). The U(IV) phases, unless colloidal, have limited solubility and mobility, while U(VI) forms many more complexes (e.g., UO_2^{2+}) of varying solubility (Cumberland et al., 2016). The most common soluble complexes are the uranyl carbonates and –hydroxyls, whereas the phosphates and silicates are more likely to precipitate and U may also complex with OM (Cumberland et al., 2018b). Pentavalent U is less well understood and might occur as an unstable intermediary, but this is unlikely to persist in the environment (Burns and Finch, 1999; Renshaw et al., 2005) or at low pH. However, metastable U(V) might be incorporated into green rust (Roberts et al., 2017).

Uranium accumulation within OM-rich sediments is thought to occur through adsorption of mobile U(VI) species onto OM functional groups followed by reduction to U(IV) (Disnar and Sureau, 1990; Hobday and Galloway, 1999; Nakashima, 1992; Nakashima et al., 1984, 1999; Sharp et al., 2011). A number of recent studies of natural samples (e.g. soils, peats and sediments) have reported U existing either in a mixed (U(IV)/U(VI) oxidation state, or predominantly as U(VI) (Cumberland et al., 2018a; Fuller et al., 2020; Mikutta et al., 2016; Regenspurg et al., 2010; Zhang et al., 2020). U(VI) complexes with OM may therefore be more stable than previously thought. Nevertheless except for colloidal forms, U(IV) is considerably insoluble and therefore immobile and the presence of non-mobile U(IV) in samples may be indicative of *in situ* U(VI) reduction to U(IV) (Cumberland et al., 2016; Wang, et al., 2013a). Direct reduction of U(VI) by lignite has been reported in the laboratory at low temperatures from 120–250°C

(Nakashima, 1992, Nakashima et al., 1984, 1999). However, the extent to which OM reduces U(VI) to U(IV) is still unconfirmed. It is therefore useful to investigate other U immobilisation mechanisms within low temperature OM-rich sediments, and their capacity to facilitate changes in U speciation. Among the factors thought to influence U(VI) to U(IV) reduction are direct enzymatic microbial reduction (Campbell et al., 2015; Newsome et al., 2014) and interaction with minerals that are sensitive to redox change (Wang et al., 2013b; Wersin et al., 1994). It has also been suggested that the reduction of U involves a combination of abiotic and biotic reactions that occur sequentially or simultaneously (Bargar et al., 2013; Bone et al., 2017; Janot et al., 2016; Noël et al., 2017). Pyrite (FeS_2) and its polymorphs have sometimes been associated with U reduction in OM–rich environments and may be sufficiently reactive to be involved in the abiotic/biotic processes mentioned above (Bonnetti et al., 2017).

1.2 Pyrite

Pyrite (cubic, FeS_2) and its polymorph, marcasite (orthorhombic, FeS_2), are common iron sulphide minerals. Other iron (II) sulphide minerals include mackinawite (FeS) and pyrrhotite. Framboidal pyrite is commonly present in low temperature sediments, particularly where there is OM, forming via either biogenic or geogenic (abiotic) processes (Gartman and Luther III, 2014; Nordstrom and Southam, 1997). Framboidal pyrite, consists of clusters of equidimensional and equimorphic micro-crystals that form a spheroidal composite grain with a larger surface area to volume ratio than cubic pyrite (Ohfuji and Rickard, 2005; Wilkin and Barnes, 1997; Wilkin et al., 1996). The terms 'framboid-like' pyrite or 'pseudo-framboids' apply when the microcrystals are non-equidimensional and non-spheroidal (Ohfuji and Rickard, 2005). Pyrite can be synthesised under a range of temperature, pressure, and chemical conditions in the laboratory (Ohfuji and Rickard, 2005). The reactivity of pyrite arises from the presence of Fe^{2+} and sulphide (S^{-}), either of which can donate electrons to become oxidised (Murphy and Strongin, 2009). A range of bivalent transition elements can substitute for Fe (Rosso and Vaughan, 2006), and other elements are incorporated as nanoscale inclusions or within the matrix, so pyrite often sequesters elements such as As, Au, Co, Cu,

93 Ni, Pb and U (Hu et al., 2016; Moreau et al., 2013). Secondary pyrite can precipitate between the
94 microcrystals (Wilkin and Barnes, 1997).

95 Co-located U and pyrite have been reported from metamorphic and sedimentary settings,
96 particularly organic-rich and pyritic shales (Och and Shields-Zhou, 2012; Schoonen, 2004), including South
97 Australian uranium mines (e.g., Beverley: Ingham et al., 2014; Wülser et al., 2011), South African gold
98 mines (e.g., Witwatersrand: England et al., 2001; Law and Phillips, 2006) and Chinese coals (Bonnetti et
99 al., 2017). Pyrite and U are also commonly co-located in roll-front deposits, which form in reducing
100 environments, with the role of pyrite as a reductant remaining infrequently reported (Min et al., 2005;
101 Renard and Beucher, 2012; Reynolds and Goldhaber, 1983; Yang et al., 2014). Under laboratory
102 conditions, U(VI) can sorb to pyrite with partial reduction of aqueous U(VI) to U(IV) and precipitation
103 of Fe(III)oxyhydroxide and/or polysulphides (Descostes et al., 2010; Eglizaud et al., 2006; Wersin et al.,
104 1994). The extent of sorption and reduction of the UO_2^{2+} ion is dependent on the pH and Eh of the
105 system and the availability of surface sites, so reduction of U(VI) to U(IV) can be incomplete (Wersin et
106 al., 1994).

107 Few studies have reported micro-scale spatial relationships between U-species and pyrite in natural
108 samples. Exceptions describe OM-poor and OM-rich environments in recent (Qafoku et al., 2009) and
109 ancient sediments (Bonnetti et al., 2017; Wülser et al., 2011). In these studies, U is reported either in a
110 mixed U(IV)/U(VI) oxidation state or as U(IV) coffinite microspheres ([$USiO_4$] or [$U(SiO_4)_{1-x}(OH)_{4x}$]),
111 interpreted as microbial in origin (Bonnetti et al., 2017; Wülser et al., 2011). However, the spatial
112 distribution of U(IV)/U(VI) at the pyrite boundary remains unconstrained, particularly within OM-rich
113 environments, and the nature of the U(IV) to U(VI) transition with increasing distance from the pyrite is
114 unknown. A more refined and spatially-constrained understanding of micro-scale U-pyrite relationships
115 would provide additional insights into the role of pyrite, and its influence on U reduction and accumulation
116 within OM-rich environments. Such knowledge is necessary for a process-based understanding of *in-situ*

or *ex-situ* U extraction from OM-rich sediments, and U stability within pyritic mining wastes and relevant pollution situations.

Here, we present a detailed investigation of a U-rich lignite (CD1577) that contains pyrite with U-rich rims from the Mulga Rock deposits, Kalgoorlie, Western Australia. The oxidation state and distribution of the U in the rims was investigated using micro-X-ray diffraction (μXRD) and synchrotron X-ray fluorescence (XFM), coupled with micro-X-ray absorption near edge spectroscopy (μXANES). As part of a mixed method approach, scanning electron microscope-energy dispersive X-ray (SEM-EDX) and transmission electron microscopy (TEM) analyses were conducted to strengthen conclusions and provide additional insights. Previous investigation of one of the sections from this sample and other powdered bulk samples from the Mulga Rock deposits using X-ray absorption spectroscopy (XAS) at the U L_3 edge revealed that U is present in a mixed oxidation state, dominated by U(VI) (71%) (Cumberland et al., 2018a). Fits to the XAS spectra were consistent with a bidentate U species, in which U(VI) is bound to carbon via two carboxyl groups. The U(IV) phase was consistent with a coffinite structure (Cumberland et al., 2018a), a phase which has been reported elsewhere within OM (Deditius et al., 2008; Leventhal et al., 1987; Min et al., 2000). However, the origin, speciation and distribution of the U(IV) identified at Mulga Rock were not elucidated by Cumberland et al. (2018a).

2 Mulga Rock deposits

Mulga Rock, located near Kalgoorlie, Western Australia (Figure 1), consists of a series of OM-rich sedimentary deposits that host U and other economic metals (e.g., Co, Cr, Cu, Ni, Pb, Ti, V, Zn, and REEs). Four orebodies make up the Mulga Rock deposits: Ambassador, Emperor, Princess and Shogun (Figure 1). Early investigations of Ambassador, discovered in 1979, indicated 13,000 tonnes of U (Douglas et al., 1993; Douglas et al., 2011). Subsequent studies uncovered U in the other three deposits. Collectively, Mulga Rock contains an estimated 66.5 Mt of ore at 520 mg kg^{-1} U_3O_8 (Vimy, 2016). The OM–rich layers at Mulga Rock also host an abundance of metals and rare earth elements (REE) in the order Ti > U > Zn > Ca > total REE > Cu > Ni > Pb > Cr > Co > Sc > V > As > Th, with total REE present in similar

7

concentrations to total U in the samples that were analysed (1-1500 ppm) (Cumberland et al., 2018a; Douglas et al., 2011).

[*Figure 1 here*]

The main ore material is an OM-rich layer, 0.5 to 2 m thick, that occurs 30–50 m below the surface; U is also present in the immediately adjacent, upper (reduced) sandy-clay layer (Figure 2). The OM-rich layers at Mulga Rock are anoxic and acidic, and likely accumulated within paleochannels and lacustrine beds that formed during the Eocene and were subsequently buried (56–34 Ma, Douglas et al., 2011). These OM-rich layers contain a mixture of woody (lignite) material combined with aquatic algal and bacterial biomass, which make up the particulate and non-particulate OM-rich fractions (Jaraula et al., 2015).

[*Figure 2 here*]

The U present at Mulga Rock likely accumulated as a result of the immobilisation of mobile U(VI) in groundwater (present day average 8 μg L^{-1} U in local groundwater) that flowed through permeable sandstones within paleochannels, and sorbed to OM where the groundwater interacted with OM-rich layers (Cumberland et al., 2018a; Douglas et al., 2011; Jaraula et al., 2015). This sorption process has been tested experimentally with U(VI) solutions, whereby U adsorbed to OM within packed columns (Cumberland et al., 2018b). The transition of the OM-rich layers and deeper sediments to anoxic conditions, led to the formation of Fe-sulphides, most likely as result of bacterial sulphate reduction (Douglas et al., 2011).

3 Materials and Methods

3.1 Sample details

The sample material originated from an archived (diamond-drilled) core extracted from the Mulga Rock Ambassador deposit in July 1988 during exploration by PNC Exploration Australia in 1979–1988 (Vimy, 2016). The sample used in this study is a lignite fragment from core CD 1577 (Ambassador, Northing 6682708.94 mS, Easting 579942.81 mE (UTM WGS84 51J), depth of core was 43.5 m). At this site, the lignite lies at depths of 37–44 metres above sandy-clay mudstones and below claystone (Figure 2). Further details of core from the Ambassador deposit are provided by Douglas et al. (2011). The U- and OM-rich layer was protected after sampling by covering the cores in plastic on site. On return from site, cores were carefully placed in a core room and stored under climate-controlled conditions at CSIRO. Selected fragments, including the fragment examined here, were encased within epoxy resin and thus protected from the air. U-rich ore fragments were selected for more detailed analysis, based on gamma counter radiography.

An epoxy-preserved sample fragment from CD1577 was selected for analysis from these archives (labelled 6101) because it displayed high gamma radiation counts. SEM imaging revealed pyrite and U-bearing minerals on the surface of the sample, with some of the latter ellipsoidal (2 × 10 μm). These ellipsoidal features were investigated further using a focussed ion beam (FIB) to produce micro sections and analysed using TEM (BIO21, University of Melbourne, Australia) and synchrotron-XFM. Thin sections were then prepared from the 6101 sample at Federation University (Ballarat, Australia), and mounted on pure quartz microscope slides to produce four mounted sub-samples 30–50 μm in thickness (slides 1–4), and one unmounted subsample of ~1 mm thickness. Reflective and transmitted light microscopy images of slides 1-4 are presented in Figure S1 to show the extent of the analytical area and the reflectance of the pyrite grains. SEM-EDX maps were performed on an edge in pyrite feature 1; and SEM-EDX maps and a μXRD transect were performed on a pyrite feature located on slide 3 (see Figure S2 for locations). The mounted thin sections were then analysed on two occasions at the Australian

9

190 Synchrotron in 2014. Early in 2014, all four thin sections were image scanned using XFM and a FIB section
191 with ellipsoidal features analysed for XANES at the U L_3 edge. Later in the same year, transects across two
192 selected pyrite features, one each from slides 1 and 2, were imaged using μXANES (Figure S1).

193

194 ## 3.2 Electron microscopy and analysis

195 SEM images and element maps were acquired using an environmental-SEM (FEI Quanta) equipped with
196 an OXFORD INCA EDX spectrometer and Gatan cold stage (BIO21, University of Melbourne,
197 Australia). The latter was used to reduce beam damage to the OM. Samples were carbon-coated to improve
198 conductivity. Images were acquired at 15 kV in backscatter using a solid state backscatter detector at 0.6
199 mbar pressure. In addition to the composite map image, the individual element map images were cross-
200 correlated to recognize inter-element relationships. To do this, each element map was converted to equal
201 pixel dimension bitmaps (8-bit) using ImageJ (Fiji); cropping where necessary. The Pearson correlation
202 coefficient was then calculated for pairs of element maps using the 'Image_CorrelationJ_1o.class' plug-in
203 (Chinga and Syverud, 2007). For these analyses, the original image size was 233 × 203 pixels, with a pixel
204 resolution of 5 μm^2. The local region size for correlation was set to three by three pixels giving the number
205 of observations as n= 5250. ImageJ produced scatterplots and a correlation (R) value, and the inbuilt R
206 software used to calculate additional statistics and the probability factor, *p,* values. Micro-sized sections of
207 ellipsoid-shaped U phases were milled using a dual beam FEI Nova Nanolab gallium ion focussed ion
208 beam (FIB) SEM equipped with EDX and Pt deposition system (BIO21, University of Melbourne). The
209 FIB-sections were placed on a Cu holey carbon mesh TEM grid and imaged using a 200 kV TEM (Tecnai
210 F20, BIO21, University of Melbourne, Australia) equipped with a scanning transmission electron
211 microscope (STEM) and EDX. Images of the FIB sections were also acquired using synchrotron X-rays
212 at the XFM beamline.

213

3.3 μXRD

Micro X-ray diffraction (μXRD) patterns were collected using a general area detector diffraction system (GADDS, Bruker) micro-diffractometer, at the Commonwealth Scientific and Research Organisation (CSIRO) laboratories in Clayton (Melbourne, Australia). The source of the X-ray beam was a Cu Kα X-ray tube operating at 40 mA, 40 kV that passed through crossed reflecting Göbel mirrors to produce a monochromatic, parallel, high-brilliance source which collimated by a 300 μm or 800 μm pinhole system. Twenty diffraction patterns were collected at 50 μm steps over a one mm transect using a 300 μm collimator (see Figure S2). Spot measurements used the 800 μm collimator. Patterns were fitted using EVA software (Bruker) and Brukers' powder diffraction file (pdf) database.

3.4 Synchrotron X-ray Fluorescence Microscopy (XFM)

Element images and μXANES were collected at the XFM beamline (Australian Synchrotron, Melbourne, Australia). It is possible to detect matrix-hosted (i.e., non-mineral) and mineral-bound U, and the beamline is suitable for analysis of complex samples that contain OM and U, at concentrations of a few ppm to wt.% (Fisher et al., 2015; Ryan et al., 2014). The measurements employed a Si(111) monochromator crystal, with a bandpass $\Delta E/E$ of approximately $1.4e^{-4}$. The monochromatized X-ray beam focusses to a spot of approximately 2 μm (Full Width at Half Maximum, FWHM) diameter using a mirror pair (Kirkpatrick-Baez, KB type) (Paterson et al., 2011). Secondary X-rays are detected at 180° from the sample using the 384-element Maia detector in a backscatter geometry (Fisher et al., 2015; Kirkham et al., 2011; Ryan et al., 2014).

Although the Maia detector is sensitive to fluorescence X-rays above ~2 keV, the low penetration of the S fluorescence (~2.4 keV) means that maps of S show S on the surface, whereas maps of the heavier elements show the average concentration over a greater depth interval within the sample. For this reason, the S map is spatially decoupled in the Z direction from maps of the heavier elements, and the relationship

11

238 between the maps is semi-quantitative at best. Furthermore, at the time of analysis, μXANES could not
239 be performed at the Australian Synchrotron XFM beamline for light elements such as S.

240 3.4.1 Element and μXANES stack image maps

241 Element maps and μXANES stack images were produced using the GeoPIXE software
242 (Etschmann et al., 2010; Li et al., 2016; Ryan, 2000; Ryan and Jamieson, 1993). Where stack images are
243 defined as image maps that also contain energy information for each excitation energy across an absorption
244 edge of a targeted element. GEOPIXE works by deconvolving the photon event stream using the dynamic
245 analysis (DA) method to project quantitative elemental images from the full spectra (Ryan, 2000; Ryan and
246 Jamieson, 1993). Following detailed XFM scanning of the element distribution (2–18.2 keV) at 2 μm, a
247 series of scans across the U L_3 edge (~17170 eV) were performed to acquire the μXANES, for selected
248 regions of interests (ROIs). In our scans, the ROIs were drawn perpendicular to the pyrite grain edges as
249 'transects'. The two transects were approximately 800 × 100 μm and 2000 × 200 μm. Each transect
250 consisted of 121 energies covering the U L_3 edge between 17000 and 17510 eV with energy steps of 15 eV
251 from 17000 to 17105 eV(pre-edge), 5 eV between 17105 and 17145 eV, 1 eV between 17150 and 17199 eV
252 (edge and white line), 2 eV between 17200 and 17268 eV, and 5 eV between 17270 and 17510 eV. The
253 position of the edge energy in the U L_3 μXANES spectrum is sensitive to the U oxidation state and, to a
254 limited extent, U species. The presence or absence of a post-white-line shoulder provides further
255 information on the species. This process produces stackable images that were used to create 4D (*x*–*y*–
256 energy–intensity) maps using GeoPIXE.

257 The μXANES spectra were extracted and exported from the 4D stacked energy scans by drawing
258 uniform-sized segments across the transect using GeoPIXE of about 73 × 70 μm or 120 × 120 μm. The
259 μXANES spectra (11 from feature one, 17 from feature two) were processed and normalised using XAS
260 analysis software (Athena, DEMETER v. 0.9.26) and then used for linear combination fitting (LCF) to
261 determine the oxidation state and species.

12

The XFM-derived spectra were aligned using XAS-derived spectra of the U mineral sub-samples where the XAS-derived spectra were acquired in both fluorescence and transmission and calibrated using a Zr foil (K-edge, E_0 = 17998 eV) to ±0.5 eV (Cumberland et al., 2018a suppl. data). The U minerals used in this study were supplied by Melbourne Museum, and included coffinite (M32495), uraninite (M26415), uranopilite (M40774) [$(UO_2)6SO_4(OH)6O_2{\cdot}14H_2O$], saleeite (M45514) [$Mg(UO_2)_2(PO_4)_2{\cdot}10H_2O$] and schoepite (M44367) [$(UO_2)_8O_2(OH)_{12}{\cdot}12(H_2O)$].

3.4.2 Linear combination fitting (LCF)

Linear combination fitting (LCF) was performed to determine the oxidation state of U using the Athena software package. Each fit used two end members, one U(IV) and one U(VI) compound. Uraninite and coffinite were used to represent the U(IV) end-member, and uranopilite, schoepite and saleeite, represented the U(VI) end-members. Uranium spectra that gave poor fits were eliminated through the process of LCF. The multiple fits using all combinations of the U(IV) and U(VI) end-members ensured that the fits were robust and that the uniqueness of the fits could be assessed. which is supported by the work of Cumberland et al. (2018) where the paths from uranopilite data, was applied to EXAFS modelling of the bulk samples.

The LCF parameters were as follows: all weights were set between zero and one and the sum of the resulting fits was forced to equal one. The fit range was from −20 eV below E_0 to +30 eV above E_0, to include the first U=O shell of U(VI) compounds (post white-line shoulder). Each LCF was performed simultaneously on a set of spectra against a pair of endmembers always returned a weighting of one. The results were plotted as bar charts to show the proportions of U(IV) and U(VI) across the transect using R packages, ggplot2 and Majick.

The LCF provides estimates of the proportions of chemical species, and has been applied to a wide range of metal compounds (Calvin, 2013). However, LCF fits to the μXANES spectra of U(VI) oxides can be challenging because the number of oxygens present in the first shell and the presence of a U=O double bond are relatively consistent across species, so the spectral shape is similar for many of the

13

vast number of known U(VI) minerals (~200, Hazen et al., 2009). Collection of high-resolution data at higher numbers in K-space can provide additional detailed information on the coordination environment through analysis of the extended X-ray absorption of the fine structure (EXAFS). It was not practical to do this at the Australian Synchrotron-XFM beamline at the time of measurement.

4 Results

4.1 Element analyses

Analyses of thin sections of lignite sample 6101 from core CD1577 via XFM revealed multiple iron- and sulphur-rich grains surrounded by extensive U-rich rims (up to ~ 500 μm) (see Figure 3). Two features were selected for detailed analysis and are hereon referenced as 'pyrite grain 1' and 'pyrite grain 2', as identified in Figure 3. Although not shown in the RGB maps, XFM element analyses revealed that rims also contained trace amounts of As and Y and the Fe-S phase also contained Co and Ni. Collected data, including traverse data extracted from XFM images show that relationships existed between Co and Ni and that neither Ni nor Co correlated with Fe or U. Complementary spot analyses of a pyrite grain located on slide 3 (see Figure S2) using μXRD fitted with a 800 μm collimator indicated that the main phase is pyrite containing minor millerite (Co, Ni S) (Figure 4). The presence of marcasite was inconclusive. As depicted in Figure S2, the grain selected for spot analysis shows an inclusion that contains Co, Ni or Zn, this feature is not considered further in this study.

[*Figure 3 here*]

[*Figure 4 here*]

14

4.2 Electron microscopy

4.2.1 SEM

The SEM–EDX analyses of the region identified which features an edge of a pyrite grain from slide 3 (see Figure S2 for location) revealed a local enrichment in C, Fe, O, S and Si (Figures 5, S3, S4). The composite image, Figure 5, shows three distinct regions are identifiable; an Fe- and S- rich region (orange), a U–O–Si-rich region (green), and a C-rich region of the sample matrix (purple-brown). Uranium is most abundant close to the edge of the pyrite grain/region and in sample cracks. The organic-rich (lignite) area around the pyrite appears light brown in reflective and transmitted light (Figure S1) and clearly surrounds the pyrite grains. The sample was preserved by C-bearing resin impregnation, so the map of C (Figure 5) should be interpreted with caution. Nevertheless, some inferences can be made; micron-sized areas of U-enrichment occur within the OM-rich area (see Figure S5), and there is no detectable C within the Fe-S area. Phosphorus, which can be an indicator of remnant microbial biomass, was only present at low concentrations. Other elements detected by EDX include trace Al, As, Co, Na, Nd, Ni, Y and Zn. In these samples, the Fe–S phase does not show a classic framboidal texture. Instead, it is similar to the framboidal-like pyrite described by Ohfuji and Rickard (2005) in that it contains micro-clusters consisting of individual crystals of 5-10 μm, which are visible in the SEM and XFM images (Figures 5, 6; and a higher resolution EDX map of pyrite grain 1 provided in Figure S6). Furthermore, mats of U-rich microcrystals were observed on other regions of the sample, see section 4.2.2 for more detail.

[*Figure 5 here*]

[*Figure 6 here*]

The composition of individual microcrystals from 'pyrite grain 1' (Figure 3A and 6B), based on semi-quantitative SEM–EDX spot analyses of the detected elements showed percent level concentrations

15

333 of C > O > S > Fe > N > Ni ≈ Co , and ppm concentrations of Si and U. The EDX analysis positioned
334 on the bright phase (Figure 6C and D) showed higher concentrations of U e.g. with percent concentrations
335 of O > S > N > Fe> Ni > U and ppm concentrations of Co > Zn ≈ Si. whereas the darker phase indicated
336 much less U with percent concentrations of O > S > N > Fe ≈ Ni > Co and ppm concentrations of Zn
337 > U > Si with U likely detected from the nearby brighter phase.

338

339 Several elements are correlated ($p < 0.001$, n = 5250), based on the SEM map data (Figure 5; Table
340 S1). Uranium is positively correlated with Si ($R^2 = 0.72$). The points on O versus U scatterplots fall into
341 two groups. In the first group, O is independent of the U concentration. In the second group, O and U
342 are positively correlated (Figure S3) and a negative correlation exists between U and C (Figure S4).

343 Iron and S are positively correlated ($R^2 = 0.88$, slope = 1.27) whereas S and U are negatively
344 correlated ($R^2 = 0.30$, $p < 0.001$). The S vs. U plot however shows a much more complicated picture: i) a
345 very steep, negative S vs. U at low S; ii) a less steep, negative S vs. U trend spanning a broad range of S
346 and U concentrations; and iii) uncorrelated showing no increase in U with increase in S. A similar pattern
347 is also observed between S and Si. The S–C scatterplot ($R^2 = 0.36$, $p < 0.001$, Figure S3) reveals two
348 populations, one showing a positive correlation and the second showing a broader negative correlation.
349 There is little S in the OM-rich matrix. Oxygen and Si portray a similar relationship to that between U and
350 O (Table S1), and is suggestive that U, Si, and O are part of the same phase. An example is the U(IV)-
351 bearing mineral coffinite ($USiO_4$). Traces of other oxides might be present but could not be resolved from
352 the data. In addition to above SEM-EDX analyses performed at three positions on a pyrite grain located
353 on slide 3 are presented in Table S2.

354 4.2.2 TEM of FIB sample

355 Mats of mineralised ellipsoids that were observed on the surface of the lignite sample prior to sub-
356 sectioning, see Figures S7 and S8, were sectioned using a FIB for further examination using TEM, and

then later by XFM. These ellipsoids were 10 μm in length by 2 μm in diameter containing U as tightly packed nanoparticles of about 10 nm, they were not located near to the larger pyrite grains, but occasionally the odd single grain was found amongst them (Figure S8 C-1). Diffraction patterns were poorly- or poly-crystalline with *d*-spacings consistent with coffinite. XFM-μXANES LCF analysis (Figure S8) also indicated coffinite in the sample. A poorly crystalline, 'non-uraninite' phase has been observed by Alessi (2014) and Bernier-Latmani et al. (2010) as a U microbial product.

4.3 μXRD

A transect taken across a pyrite boundary using μ-XRD, illustrated in Figure S2, revealed two distinct mineral phases, pyrite and coffinite (Figure 7). The spectrum in Figure 7b indicated 81–100% cubic pyrite (a = b = c = 5.441 Å), but due to high background counts, the presence of other minerals, for example millerite and marcasite, could not be easily determined. The pattern lacks peaks around 45-55° 2θ indicating that marcasite and millerite are either present in low quantities or absent entirely. Other phases which could be present as residuals of reaction products, e.g. iron oxide (Fe_2O_3, PDF-00-005-0637), greigite (Fe_3S_4, PDF 089-1998), sphalerite (Zn, FeS) and coffinite, were not identified. The μXRD pattern is inconsistent with the presence of U(VI) oxide and uraninite. Coffinite (PDF-00-011-0420) (tetragonal, a = b = c = 6.979, h,k,l = 2,0,0) is the only phase that can explain the main μXRD peaks (~95.7%) (Figure 7c), but U(VI) oxide (e.g., UO_3: PDF 00-011-0420, hexagonal, a = b = 3.971, c = 4.168 Å, h,k,l = 2,0,0) also fits under the broader peaks which may explain the remaining ~4.3% of the fit in Figure 7c. It is noteworthy that uraninite (UO_2, PDF 00-047-1879) was not a feasible fit to the spectra of Figure 7c.

[Figure 7 here]

17

4.4 Synchrotron XFM-μXANES

Synchrotron XFM RGB (Fe, S, U) element, maps of Fe, S and U, LCF U(IV):U(VI) ratios, and element concentrations for two analysed pyrite grains as a function of the position on the transect were plotted (Figures 8, 9). XANES spectra along with their fits as dotted lines are shown in Figure S9. The LCFs for both pyrite grains using two U end members gave similar results irrespective of the choice of U(IV) mineral (coffinite or uraninite), and with U(VI) represented by uranopilite (Table 1). Four tests were performed: test 1 modelled pyrite grain 1 using coffinite and uranopilite; test 2 modelled pyrite grain 1 using uraninite and uranopilite; test 3 modelled pyrite grain 2 using coffinite and uranopilite; and test 4 modelled pyrite grain 2 using uraninite and uranopilite. Uranopilite was the preferred U(VI) end-member because S is present in the sample, and LCFs using the other U(VI) minerals gave inconsistent results and the calculated proportions are negative. Therefore, it is likely that the U(VI) end-member was sulphate-bearing, but it is not possible to identify the end-member with confidence. The mean of the relative error on the LCF (relative error = $\Sigma((\text{data} - \text{fit})^2)/\Sigma(\text{data}^2)$; Calvin, 2013) was less than 2%. The uncertainties for test 1 are ± 13% for uranopilite and ±4% for coffinite, for test 2, ±15% for uranopilite and ±8% for uraninite, for test 3, ± 12% for uranopilite and ± 3% for coffinite, and for test 4, ± 6% for uranopilite and ± 3% for uraninite.

The U concentration is highest at the edge of the pyrite grains (Figures 8d, 8f, 9d, 8f) and most U is in the U(IV) oxidation state, based on the μXANES LCF analysis. The proportion of U(IV) decreases with increasing distance from the pyrite margin towards the matrix. In Figure 9 the trend shows a clear decline from 100% U(IV) to 16% in segments #13 to #17 whereas in Figure 8 the U(IV) initially shows a decrease from 100% to 19% in segments #6 to #10 but then slightly increases in segment #11 to 27%. U within the pyrite grains recorded a mix of oxidation states where U concentrations are lower, but significant at ~0.3 to 0.5 wt.% for fluorescent XANES measurements (Figures 8, 9). The XFM analyses of non-pyrite areas show that U is disseminated throughout the matrix (Figure S3 and Figure S5). Carbon is not detected

18

by XFM, however details of the matrix can be depicted in the individual element maps including U, which indicates that U is disseminated throughout the matrix.

[Figure 8 here]

[Figure 9 here]

[Table 1 here]

5 Discussion

5.1 Uranium and pyrite within organic matter-rich sediments

Pyrite is commonly found in reduced OM environments, such as recent and ancient wetlands and coals (Bonnetti et al., 2015; 2017). The formation of pyrite requires a highly reduced form of sulphur (e.g., HS^-, H_2S) that may be supplied via sulphate-reducing bacteria (Southam and Saunders, 2005). Framboidal pyrite occasionally contains other sulphide phases such as millerite and marcasite as might be suggested by the μXRD patterns presented here. At Mulga Rock, the OM-U-rich layers were likely formed at low temperature with a low pH and fluctuating redox conditions. Such an environment might therefore suggest the possibility of other sulphide phases juxtaposed with micro grains of the framboidal-like pyrite (Douglas et al., 2011; Ohfuji and Rickard, 2005; Reynolds and Goldharbour, 1983).

The U within Mulga Rock samples was likely sequestered as U(VI) from groundwater through adsorption to OM functional groups (Cumberland et al., 2018a; b). A previous study of the U-OM relationship on Mulga Rock samples showed that U is finely dispersed within the OM, existing as a mix of U(VI) and U(IV), predominantly as U(VI) (Cumberland et al., 2018a). EXAFS scans performed on Mulga Rock bulk cores indicated that the U(VI) was likely in monomeric form bound with carboxylic acid groups of humic compounds, with spectral patterns analogous to U-humics reported by Denecke et al., (1998) and Kaplan et al., (2016). A non-pyritic section of sample 6101, the focus of the present study, was

19

previously investigated using XAS by Cumberland et al. (2018a). The 6101 EXAFS spectra taken from six blind locations revealed two oxidation states, a reduced U of mineralised coffinite, and an oxidised U similar to Mulga Rock bulk core samples (Cumberland et al., 2018a). In another study, plant sourced OM highly rich in aromatics within a column, could rapidly adsorb U(VI) without reduction (Cumberland et al., 2018b). Only where U adsorbed to (non-sterile) cotton wool bungs did partial reduction of U(VI) to U(VI) occur (Cumberland et al., 2018b). Fuller et al. (2020) reported U(VI) complexation to organic rich sediments at Needle's Eye, UK, noting that a reduced non-crystalline U only existed where sediments were organic poor and sulphate reducing. An explanation postulated was that the U(VI)-OM complexes are stable against reduction to U(IV) for prolonged periods irrespective of local conditions (Fuller et al., 2020). Other constituents, such as pyrite or microbial influences, within the sediments might be necessary for in situ reduction to U(IV), and which might not be complexed to OM because local OM sites are already saturated with U.

Geochemical models (e.g., PHREEQC, Geochemist's workbench) suggested that given a wide availability of ligands, a range of UO_2^{2+} species may be present at low pH/high Eh, in particular, $U(VI)O_2SO_4$ (Cumberland et al., 2016). In the same work, a U-humate species, representing OM, incorporated into the model was prevalent between pH 3 and 6.5. Uraninite is the precipitating phase over a range of pH and at low Eh, however increasing the amount of dissolve silica, results in coffinite precipitation instead of uraninite (Cumberland et al., 2016). Cumberland et al. (2018b), showed that in a WHAM-VI model output, UO_2^{2+} adsorbs to quartz above pH 5 to ~8. The addition of particulate humic acid, changes the behaviour of UO_2^{2+} adsorption to quartz and instead preferentially binds to OM across a wider pH range of 4 to 10 (Cumberland et al. 2018b). Higher surface charge from humics was one likely explanation (Cumberland et al., 2018b).

While U-pyrite associations have been observed under laboratory conditions, few studies have reported this in natural samples and the extent to which U crusts can form remains controversial. Yang et

20

al. (2014) considered that abiotic sorption of U onto pyrite was not viable, however previous studies have shown that surface sorption of UO_2^{2+} could occur on pyrite, inferring that sorption was facilitated by the negative surface charge of pyrite at pH > 2 (Descostes et al., 2010; Wersin et al., 1994). The electrochemical properties of pyrite were also explored by Möller and Kersten (1994), demonstrating that gold could accumulate on pyrite-type surfaces when in electrolyte solutions. The distribution of the gold in the Möller and Kersten (1994) study mainly occurred at the cathode where the gold was reduced from Au^+ to Au^0. While this process is unexplored in the Mulga Rock samples, it is interesting to note that the U surrounding the large pyrite grain shown on slide 3 appears to be greater at each end of the grain (Figure 1, 2). None of these studies included OM and while simple sorption cannot be excluded, the OM in our samples might be facilitating sorption of UO_2^{2+} to pyrite to 100's of microns thick. Understanding these occurrences and interactions have implications for management of U fate in mining activities, waste storage and contaminated land.

5.2 Uranium reduction process

The observed thickness of reduced U on the Mulga Rock sample shows that U might be reduced even if it is not in direct contact with pyrite and thus might not be surface-limited. The implications of this observation are significant, because previously U(IV) has only been observed as an uneven discontinuous coating on (cubic) pyrite surfaces (Descostes et al., 2010; Qakfoku et al., 2009; Scott et al., 2007; Wersin et al., 1994). The condition of these pyrite surfaces such as age and the limited number of defect sites, may contribute to unevenness and heterogeneity of such sorption (Scott et al., 2007; Wersin et al., 1994). The surfaces of framboidal pyrites, (and marcasite), are rougher and might provide a large number of adsorption and reaction sites, compared to cubic pyrite, enabling more effective U(VI) reduction (Hu et al., 2016; Murowchick and Barnes, 1996; Qafoku et al., 2009; Reynolds and Goldhaber, 1983). In addition to simple sorption and reduction processes, the replacement of minerals at the surface through dissolution and precipitation is described for a wide range of systems that could also result in mineral surface crusts which in turn diminished the host mineral, e.g. pyrite (Fang et al., 2009; Putnis, 2009).

21

In addition to U on the perimeter of the framboidal-like pyrite, the presence of traces of U within pyrite, might indicate that there is porosity between the microcrystals for an interstitial phase of U to exist (Figure 6). Townsend et al. (2019) recently reported that a U(VI)-persulfate might form a transient phase during the reduction of ferrihydrite to form mackinawite. However, the longevity of such a transient phase remains uncertain. The existence of U(V) as an intermediary oxidation state is more uncertain as U(V) species are short-lived and analytically difficult to recognise at the L_3 edge, although U(V) might be resolved at the M_4 edge (Fuller et al., 2020). Fuller et al. (2020) examined OM-U-rich samples from Needle's Eye in Scotland using the M_4 edge, but the presence of U(V) was not detected.

Here, we propose two possible explanations for the thick U(IV) rim, assuming that U(VI) is reduced to U(IV) in situ: (1) the youngest U(IV) occurs on the outer perimeter of the concentrated U rim that surrounds pyrite; in this case electrons donated by pyrite are transported to the youngest U, with the implication that both pyrite and U(IV) acts as semiconductors; or, (2) the youngest U(IV) grows on the pyrite surface, with pyrite consumption continually releasing new sites for U(VI)-pyrite reactions.

In (1), it is postulated that the pyrite can drive U reduction remotely from the pyrite surface. Rimstidt and Vaughan (2003) note that pyrite is a semi-conductor so electron transfer can occur across grains to supply reactions at other sites. They propose that oxidation of Fe(II) to Fe(III) takes place, but that the Fe(III) state is cathodic and temporary because electrons produced by oxidation of S_2^{2-} oxidation reduce Fe(III) back to Fe(II). Sulphide, S_2^{2-}, oxidation on the other hand is a multi-step process that can supply up to seven electrons (Rimstidt and Vaughan, 2003). Electrons produced by S may drive reduction of U(VI) beyond the immediate boundary of the pyrite, aided by the semi-conduction properties of $USiO_4$. Labile, reactive OM, whether lignite or extracellular biomass, in the Mulga Rock sample, may also facilitate electron transfer. While the reaction could be feasible, it is inconsistent with the observed shape of the pyrite and the presence of U found between the micro-crystals. The observations made by Wersin et al. (1994) are less supportive of this theory whereby they noted that reduction of sorbed uranyl was limited to fresh reaction sites at pyrite surfaces. More recently however, Townsend et al. (2020) reported a new

observed U(VI)-persulphide phase, though its longevity is unknown. No pyrite oxidation products were observed in the current study, and further detailed investigation into such products are required for future studies.

In support of explanation (2), an inward reaction pathway at the surface of the pyrite, numerous researchers have proposed the oxidation of Fe^{2+} to Fe^{3+} with simultaneous reduction of UO_2^{2+} to UO_{2-x} (Boland et al., 2014, Du et al., 2011, Latta et al., 2012, O'Loughlin et al., 2003; Percak-Dennett et al., 2014; Scott et al., 2007) and the production of S as sulphates or polysulphides (Descostes et al., 2010; Sachs et al., 2010); although S products can only be speculated here. In the literature, the end-product in reactions between U and pyrite are often written for uraninite (e.g. Scott et al., 2007), however coffinite is reported in samples from OM-rich environments, and this work proposes a mixture of coffinite and uraninite as end-products (e.g. Bonnetti, 2015, 2017; Deditius, 2008; Leventhal, 1987). The formation of coffinite in addition to uraninite requires the availability of dissolved silica supplied either from groundwater or via bacterial processes (Southam and Saunders, 2005). Coffinite formation processes are poorly constrained (Guo et al., 2015; Mesbah et al., 2015) and Guo et al. (2015) proposes the reversible reaction; $USiO_{4[s]} + 2H_2O_{(l)} \leftrightarrow UO_{2[s]} + Si(OH)_{4[aq]}$, in which coffinite may be metastable with respect to uraninite and silicate. Additional electrons provided by OM and/or microbes maybe important for coffinite formation to meet the conditions of the above reaction (Dedituis et al., 2008; Nakashima, 1992a). A pathway previously proposed by Nakashima (1992b) involves R, as an OM residual group, reacting with U for binding. Such that U and OM might react with dissolved silica to form coffinite, for example; $RH_2 + UO_2^{2+} + Si(OH)4 \leftrightarrow R + USiO4 + 6H^+$. Evidence of the action of microbes with coffinite formation is not substantiated in the Mulga Rock samples, however the observation of randomly orientated coffinite-rich ellipsoids seen in Figures S7 and S8 raise doubts about purely geogenic processes.

In further support of explanation (2), the potential for U(IV) to accumulate whilst the pyrite is simultaneously consumed is illustrated by the element map shown in Figure S10, where relatively wide zones of U(IV), ~500μm wide, surround small pyrite grains, <50 μm diameter. This reaction requires a

23

527 continuous supply of groundwater-derived UO_2^{2+} to the reaction sites. The size of U(IV) rims in the
528 images, extend from 20 to 600 μm, however it could be speculated that the U(IV) might mark the original
529 extent of the pyrite. This mechanism is comparable to the replacement of minerals by dissolution and
530 precipitation, described by Putnis (2009) and Fang et al. (2009), and is consistent with the U found between
531 the micro-crystals of the framboids.

532 ## 5.3 Microbes, uranium, pyrite and OM.

533 It has long been recognised that biogenic U reduction via direct enzymatic reduction (e.g., bacteria,
534 fungi) can occur under laboratory conditions (Suzuki et al., 2002), mediated by *Shewanella oneidensis*, and in
535 acetate and various amended sediments (Alessi et al., 2014; Bargar et al., 2013; Bernier-Latmani, et al.,
536 2010; Suzuki et al., 2002). If the U-rich ellipsoids, observed within the lignite sample prior to sectioning,
537 are either microbial in origin or have occurred as a result of microbial action (see Figure S7 and 8), this
538 might suggest a link between the reduced U, pyrite and OM. The diffraction patterns for coffinite within
539 the ellipsoids showed an untypically poorly or poly-crystalline structure. Uraninite phases, not conforming
540 to a typical uraninite structure have been associated with microbial U reduction (Bernier-Latmani et al.,
541 2010). However, no such findings are reported for coffinite.

542 Bacteria have been shown to be pivotal in the reduction of U(VI) to U(IV) in roll-front deposits
543 (Bhattacharyya et al., 2016; Bone at al., 2017). Bone et al. (2017) demonstrated that U(VI) reduction to
544 U(IV) occurred in a non-sterile organic sample but reduction did not occur in a system otherwise identical
545 but sterile, indicating that the role of microbes could be feasible within natural settings. However, in our
546 sample, concentrations of U-rich ellipsoids were not viewed near our studied pyrite grains and might
547 constitute a different process of electron exchange. For example, if microbes were present they could be
548 capable of mediating the dissolution of mineralised silica, which is required for coffinite formation, while
549 other process drive pyrite formation e.g. via sulphate-reducing bacteria (Southam and Saunders, 2005). In
550 a study investigating the reduction of U(VI) by microbes and pyrite, Behrends and Van Cappellen (2005)
551 showed that *S. putrefaciens* most likely reduced Fe(III) to Fe(II) first, and Fe(II) then donated electrons to

24

552 drive reduction of U(VI) to U(IV). Both processes may involve OM, which is utilised by microbes to
553 produce organic acids that can dissolve the silica and/or the metals (Southam and Saunders 2005). As part
554 of their actions, microbes may facilitate the complexing of metals to OM to achieve self-preservation
555 (Southam and Saunders, 2005). Collectively OM, metal and microbes could produce the conditions that
556 facilitated formation of the observed textures at Mulga Rock. Thus, microbial activity might have played a
557 role in U(VI) reduction at Mulga Rock, but does not point to the exact process that occurred at the edge
558 of the pyrite. The complexity of the mechanisms examined here highlights the complexity and variability
559 of the redox state of U and chemical speciation for U-OM associations in modern sediments (Bone et al.,
560 2017; Mikutta et al., 2016). In our samples, the formation of framboidal-like pyrite could have formed
561 biogenically or geogenically. Whilst the former might have occurred , the subsequent reduction of U(VI)
562 to U(IV) was likely primarily driven by pyrite oxidation, but the role of bacteria cannot be discounted.
563 Further study is required to disentangle the possible pathways between U, OM, pyrite and microbes.

564 # 6 Conclusion

565 In this work we show in high resolution using SEM and XFM, natural formations of U-rich rims (~100
566 microns) on framboidal-like pyrite within OM sediments. Results of multi-method analyses of U using
567 μXRD, XFM and μXANES are consistent with a U(IV) phase which is predominantly coffinite mixed
568 with uraninite. Further analyses of the U rim reveals a progression to U(VI) with increasing distance away
569 from the edge of the pyrite. This suggests that U(VI) was reduced to U(IV). We further suggest that the
570 reduction reaction was likely occurring at the interface between the pyrite and reduced U phase and that
571 the direction of the reaction progressed towards the pyrite resulting in the pyrite grain diminishing. The
572 presence of U between the micro-crystals and the shape of the framboidal-like pyrite is supportive of U
573 being mobilised to the pyrite which was then reduced at its edge. This proposes the notion that framboidal-
574 like pyrite immobilises aqueous U(VI) through reduction to U(IV) in OM-bearing deposits. The presence
575 of U-rich microfossils found on another part of the sample using SEM-FIB and TEM, away from the
576 framboidal-like pyrite grains, indicates that U(VI) was reduced to U(IV) but though another mechanism

to pyrite. This work is relevant for understanding the stability of U in industrial mining and tailing and environmental management. Further study however is required to disentangle the processes that may occur between U, OM, pyrite and microbes.

7 Acknowledgements

This work was funded through a grant to JWM and KAE from the CSIRO Organic Geochemistry of Mineral Systems (OGMS) Research Cluster. Parts of this research were undertaken on the XAS and XFM beamline at the Australian Synchrotron, part of ANSTO. We would like to thank: Xavier Moreau (Vimy Resources) for Mulga Rock samples; Dr David Paterson for beamline assistance at AS XFM; Dr David Hay for GADDS Micro-XRD at CSIRO; Dr Sergey Rubanov and Roger Curtain at Bio21, University of Melbourne; Museum Victoria (Melbourne) for uranium minerals, Dr Jason Kirby (CSIRO) for his valuable comments; and Dr Steven Henderson and Dr Keith Torrance for editorial contributions. SC would like to thank the Australian Synchrotron (AS) for beamtime R1-2015-8840.

8 References

Alessi, D.S., Lezama-Pacheco, J.S., Janot, N., Suvorova, E.I., Cerrato, J.M., Giammar, D.E., Davis, J.A., Fox, P.M., Williams, K.H., Long, P.E., Handley, K.M., Bernier-Latmani, R. and Bargar, J.R., 2014. Speciation and Reactivity of Uranium Products Formed during in Situ Bioremediation in a Shallow Alluvial Aquifer. Environmental Science & Technology, 48(21): 12842-12850.

Bayliss, P, 1977. Crystal structure refinement of a weakly anisotropic pyrite cubic model. Database_code_amcsd_605. American Mineralogist (62) 1168-1172.

Bargar, J.R., Williams, K.H., Campbell, K.M., Long, P.E., Stubbs, J.E., Suvorova, E.I., Lezama-Pacheco, J.S., Alessi, D.S., Stylo, M., Webb, S.M., Davis, J.A., Giammar, D.E., Blue, L.Y. and Bernier-Latmani, R., 2013. Uranium redox transition pathways in acetate-amended sediments. Proceedings of the National Academy of Sciences, 110(12): 4506-4511.

26

601 Behrends, T. and Van Cappellen, P. (2005) Competition between enzymatic and abiotic reduction
602 of uranium(VI) under iron reducing conditions. Chemical Geology 220: 315-327.

603 Bernier-Latmani, R., Veeramani, H., Vecchia, E.D., Junier, P., Lezama-Pacheco, J.S., Suvorova,
604 E.I., Sharp, J.O., Wigginton, N.S. and Bargar, J.R. (2010) Non-uraninite Products of Microbial U(VI)
605 Reduction. Environmental Science & Technology 44, 9456-9462.

606 Bhattacharyya, A., Campbell, K.M., Kelly, S.D., Roebbert, Y., Weyer, S., Bernier-Latmani, R. and
607 Borch, T. (2017) Biogenic non-crystalline U(IV) revealed as major component in uranium ore deposits.
608 Nature Communications 8: 15538.

609 Boland, D.D., Collins, R.N., Glover, C.J., Payne, T.E. and Waite, T.D. (2014) Reduction of U(VI)
610 by Fe(II) during the Fe(II)-Accelerated Transformation of Ferrihydrite. Environmental Science &
611 Technology 48: 9086-9093.

612 Bone, S.E., Dynes, J.J., Cliff, J. and Bargar, J.R. (2017) Uranium(IV) adsorption by natural organic
613 matter in anoxic sediments. Proceedings of the National Academy of Sciences 114, 711–716.

614 Bonnetti, C., Cuney, M., Malartre, F., Michels, R., Liu, X. and Peng, Y., 2015. The Nuheting
615 deposit, Erlian Basin, NE China: Synsedimentary to diagenetic uranium mineralization. Ore Geology
616 Reviews, 69(0): 118-139.

617 Bonnetti, C., Liu, X., Zhaobin, Y., Cuney, M., Michels, R., Malartre, F., Mercadier, J. and Cai, J.,
618 2017. Coupled uranium mineralisation and bacterial sulphate reduction for the genesis of the Baxingtu
619 sandstone-hosted U deposit, SW Songliao Basin, NE China. Ore Geology Reviews, 82: 108-129.

620 Burns, P.C. and Finch, R.J. (1999) Wyartite: crystallographic evidence for the first pentavalent-
621 uranium mineral. American Mineralogist 84, 1456-1460.

622 Calvin, S., 2013 Xafs for everyone. CRC Press, Taylor and Francis. pp 449. ISBN 13: 978-1-
623 4398-7864-4

624 Campbell, K.M., Gallegos, T.J. and Landa, E.R., 2015. Biogeochemical aspects of uranium
625 mineralization, mining, milling, and remediation. Applied Geochemistry, 57: 206-235.

626 Chinga, G. and Syverud, K., 2007. Quantification of paper mass distributions within local picking
627 areas. Nordic Pulp and Paper Res J, 22(4): 441-446.

628 Cumberland, S.A., Douglas, G., Grice, K. and Moreau, J.W., 2016. Uranium mobility in organic
629 matter-rich sediments: A review of geological and geochemical processes. Earth-Science Reviews, 159:
630 160-185.

631 Cumberland, S.A., Etschmann, B., Brugger, J., Douglas, G., Evans, K., Fisher, L., Kappen, P. and
632 Moreau, J.W., 2018a. Characterization of uranium redox state in organic-rich Eocene sediments.
633 Chemosphere, 194: 602-613.

634 Cumberland, S.A., Wilson, S.A., Etschmann, B., Kappen, P., Howard, D., Paterson, D. and
635 Brugger, J., 2018b. Rapid immobilisation of U(VI) by Eucalyptus bark: Adsorption without reduction.
636 Applied Geochemistry, 96: 1-10.

637 Deditius, A.P., Utsunomiya, S. and Ewing, R.C., 2008. The chemical stability of coffinite,
638 USiO4.nH(2)O; 0<n<2, associated with organic matter: A case study from Grants uranium region, New
639 Mexico, USA. Chemical Geology, 251(1-4): 33-49.

640 Denecke, M.A., Reich, T., Pompe, S., Bubner, M., Heise, K.H., Nitsche, H., Allen, P.G., Bucher,
641 J.J., Edelstein, N.M., Shuh, D.K. and Czerwinski, K.R. 1998 EXAFS investigations of the interaction of
642 humic acids and model compounds with uranyl cations in solid complexes. Radiochimica Acta 82, 103-
643 108.

644 Descostes, M., Schlegel, M.L., Eglizaud, N., Descamps, F., Miserque, F. and Simoni, E., 2010.
645 Uptake of uranium and trace elements in pyrite (FeS2) suspensions. Geochimica et Cosmochimica Acta,
646 74(5): 1551-1562.

647 Disnar, J.R. and Sureau, J.F., 1990. Organic matter in ore genesis: Progress and perspectives.
648 Organic Geochemistry, 16(1–3): 577-599.

649 Douglas, G.B., Butt, C.R.M. and Gray, D.J., 2011. Geology, geochemistry and mineralogy of the
650 lignite-hosted Ambassador palaeochannel uranium and multi-element deposit, Gunbarrel Basin, Western
651 Australia. Mineralium Deposita, 46(7): 761-787.

652 Douglas, G.B., Gray, D.J. and Butt, C.M. (1993) Geochemistry, minerology and
653 hydrogeochemistry of the Ambassador multi-element lignite deposit, Western Australia: With additional
654 investigations on the characterization of organic matter. CSIRO, Australia.

655 Du, X., Boonchayaanant, B., Wu, W.-M., Fendorf, S., Bargar, J. and Criddle, C.S. (2011) Reduction
656 of Uranium(VI) by Soluble Iron(II) Conforms with Thermodynamic Predictions. Environmental Science
657 & Technology 45, 4718-4725.

658 Eglizaud, N., Miserque, F., Simoni, E., Schlegel, M. and Descostes, M., 2006. Uranium(VI)
659 interaction with pyrite (FeS2): Chemical and spectroscopic studies, Radiochimica Acta, pp. 651.

660 England, G.L., Rasmussen, B., Krapež, B. and Groves, D.I., 2001. The Origin of Uraninite,
661 Bitumen Nodules, and Carbon Seams in Witwatersrand Gold-Uranium-Pyrite Ore Deposits, Based on a
662 Permo-Triassic Analogue. Economic Geology, 96(8): 1907-1920.

663 Etschmann, B.E., Ryan, C.G., Brugger, J., Kirkham, R., Hough, R.M., Moorhead, G., Siddons,
664 D.P., De Geronimo, G., Kuczewski, A., Dunn, P., Paterson, D., de Jonge, M.D., Howard, D.L., Davey, P.
665 and Jensen, M., 2010. Reduced As components in highly oxidized environments: Evidence from full
666 spectral XANES imaging using the Maia massively parallel detector. American Mineralogist, 95(5-6): 884-
667 887.

668 Evangelou, V.P. and Zhang, Y.L., 1995. A review: Pyrite oxidation mechanisms and acid mine
669 drainage prevention. Critical Reviews in Environmental Science and Technology, 25(2): 141-199.

Evans, K.A., Gandy, C.J. and Banwart, S.A., 2003. Mineralogical, numerical and analytical studies of the coupled oxidation of pyrite and coal. Mineralogical Magazine, 67(2): 381-398.

Xia, F., Brugger, J., Chen, G., Ngothai, Y., O'Neill, B., Putnis, A. and Pring, A. (2009) Mechanism and kinetics of pseudomorphic mineral replacement reactions: A case study of the replacement of pentlandite by violarite. Geochimica et Cosmochimica Acta 73, 1945-1969.

Fisher, L.A., Fougerouse, D., Cleverley, J.S., Ryan, C.G., Micklethwaite, S., Halfpenny, A., Hough, R.M., Gee, M., Paterson, D., Howard, D.L. and Spiers, K., 2015. Quantified, multi-scale X-ray fluorescence element mapping using the Maia detector array: application to mineral deposit studies. Mineralium Deposita, 50(6): 665-674.

Fuchs, L.H, Gebert, E, 1958. X-ray studies of synthetic coffinite, thorite and uranothorites. Database_code_amcsd_83. American Mineralogist. 43: 243-248.

Fuller, A.J., Leary, P., Gray, N.D., Davies, H.S., Mosselmans, J.F.W., Cox, F., Robinson, C.H., Pittman, J.K., McCann, C.M., Muir, M., Graham, M.C., Utsunomiya, S., Bower, W.R., Morris, K., Shaw, S., Bots, P., Livens, F.R. and Law, G.T.W. (2020) Organic complexation of U(VI) in reducing soils at a natural analogue site: Implications for uranium transport. Chemosphere 254, 126859.

Gartman, A. and Luther III, G.W., 2014. Oxidation of synthesized sub-micron pyrite (FeS2) in seawater. Geochimica et Cosmochimica Acta, 144(0): 96-108.

Greenwood, P., Brocks, J., Grice, K., Schwark, L., Jaraula, C., Dick, J. and Evans, K. (2013) Organic Geochemistry and Mineralogy: I. Characterisation of Organic Matter Associated with Metal Deposits. Ore Geology Reviews, 1-27.

Guo, X., Szenknect, S., Mesbah, A., Labs, S., Clavier, N., Poinssot, C., Ushakov, S.V., Curtius, H., Bosbach, D., Ewing, R.C., Burns, P.C., Dacheux, N. and Navrotsky, A. (2015) Thermodynamics of formation of coffinite, USiO4. Proceedings of the National Academy of Sciences 112, 6551-6555.

693 Hansley, P.L. and Spirakis, C.S., 1992. Organic matter diagenesis as the key to a unifying theory
694 for the genesis of tabular uranium-vanadium deposits in the Morrison Formation, Colorado Plateau.
695 Economic Geology, 87(2): 352-365.

696 Hazen, R.M., Ewing, R.C. and Sverjensky, D.A. (2009) Evolution of uranium and thorium
697 minerals. American Mineralogist 94, 1293-1311.

698 Hobday, D.K. and Galloway, W.E., 1999. Groundwater processes and sedimentary uranium
699 deposits. Hydrogeology Journal, 7(1): 127-138.

700 Hu, S.-Y., Evans, K., Fisher, L., Rempel, K., Craw, D., Evans, N.J., Cumberland, S., Robert, A.
701 and Grice, K., 2016. Associations between sulfides, carbonaceous material, gold and other trace elements
702 in polyframboids: Implications for the source of orogenic gold deposits, Otago Schist, New Zealand.
703 Geochimica et Cosmochimica Acta, 180: 197-213.

704 Ingham, E.S., Cook, N.J., Cliff, J., Ciobanu, C.L. and Huddleston, A., 2014. A combined chemical,
705 isotopic and microstructural study of pyrite from roll-front uranium deposits, Lake Eyre Basin, South
706 Australia. Geochimica et Cosmochimica Acta, 125(0): 440-465.

707 Janot, N., Lezama Pacheco, J.S., Pham D.Q., O'Brien, T.M., Hausladen, D., Noël, V., Lallier, F.
708 Maher, K., Fendorf, S., Williams, K.H, Long, P.E, and Bargar, J.R. 2016. Physico-Chemical Heterogeneity
709 of Organic-Rich Sediments in the Rifle Aquifer, CO: Impact on Uranium Biogeochemistry.
710 Environmental Science and Technology, 50, 46−53

711 Jaraula, C.M.B., Schwark, L., Moreau, X., Pickel, W., Bagas, L. and Grice, K., 2015. Radiolytic
712 alteration of biopolymers in the Mulga Rock uranium deposit. Applied Geochemistry, 52: 97-108.

713 Kirkham, R., Dunn, P.A., Kuczewski, A.J., Siddons, D.P., Dodanwela, R., Moorhead, G.F., Ryan,
714 C.G., De Geronimo, G., Beuttenmuller, R., Pinelli, D., Pfeffer, M., Davey, P., Jensen, M., Paterson, D.J.,
715 de Jonge, M.D., Howard, D.L., Küsel, M. and McKinlay, J. (2011), The Maia Spectroscopy Detector

System: Engineering for Integrated Pulse Capture, Low-Latency Scanning and Real-Time Processing, AIP Conf. Proc. 2011, 1234, 240−243. http://scitation.aip.org/content/aip/proceeding/aipcp/10.1063/1.3463181

Langmuir, D. (1978) Uranium solution-mineral equilibria at low temperatures with applications to sedimentary ore deposits. Geochimica et Cosmochimica Acta 42: 547-569.

Latta, D.E., Boyanov, M.I., Kemner, K.M., O'Loughlin, E.J. and Scherer, M.M. (2012) Abiotic reduction of uranium by Fe(II) in soil. Applied Geochemistry 27: 1512-1524.

Law, J. and Phillips, N., 2006. Witwatersrand gold-pyrite-uraninite deposits do not support a reducing Archean atmosphere. Geological Society of America Memoirs, 198: 121-141.

Le Pape, P., Blanchard, M., Brest, J., Boulliard, J.-C., Ikogou, M., Stetten, L., Wang, S., Landrot, G. and Morin, G. (2017) Arsenic Incorporation in Pyrite at Ambient Temperature at Both Tetrahedral S–I and Octahedral FeII Sites: Evidence from EXAFS–DFT Analysis. Environmental Science & Technology 51, 150-158.

Leventhal, J.S., Grauch, R.I., Threlkeld, C.N., Lichte, F.E. and Harper, C.T., 1987. Unusual organic matter associated with uranium from the Claude Deposit, Cluff Lake, Canada. Economic Geology, 82(5): 1169-1176.

Li, K., Etschmann, B., Rae, N., Reith, F., Ryan, C.G., Kirkham, R., Howard, D., Rosa, D.R.N., Zammit, C., Pring, A., Ngothai, Y., Hooker, A. and Brugger, J., 2016. Ore Petrography Using Megapixel X-Ray Imaging: Rapid Insights into Element Distribution and Mobilization in Complex Pt and U-Ge-Cu Ores. Economic Geology, 111(2): 487-501.

Lindsay, M.B.J., Moncur, M.C., Bain, J.G., Jambor, J.L., Ptacek, C.J. and Blowes, D.W., 2015. Geochemical and mineralogical aspects of sulfide mine tailings. Applied Geochemistry, 57(Supplement C): 157-177.

739 Mesbah, A., Szenknect, S., Clavier, N., Lozano-Rodriguez, J., Poinssot, C., Den Auwer, C., Ewing,
740 R.C. and Dacheux, N. (2015) Coffinite, USiO4, Is Abundant in Nature: So Why Is It So Difficult To
741 Synthesize? Inorganic Chemistry 54, 6687-6696.

742 Mikutta, C., Langner, P., Bargar, J.R. and Kretzschmar, R., 2016. Tetra- and Hexavalent Uranium
743 Forms Bidentate-Mononuclear Complexes with Particulate Organic Matter in a Naturally Uranium-
744 Enriched Peatland. Environmental Science & Technology, 50(19): 10465–10475.

745 Min, M., Xu, H., Chen, J. and Fayek, M., 2005. Evidence of uranium biomineralization in
746 sandstone-hosted roll-front uranium deposits, northwestern China. Ore Geology Reviews, 26(3–4): 198-
747 206.

748 Min, M.Z., Meng, Z.W., Sheng, G.Y., Min, Y.S. and Liu, X., 2000. Organic geochemistry of
749 paleokarst-hosted uranium deposits, South China. Journal of Geochemical Exploration, 68(3): 211-229.

750 Möller, P. and Kersten, G. 1994 Electrochemical accumulation of visible gold on pyrite and
751 arsenopyrite surfaces. Mineralium Deposita 29, 404-413.

752 Moncur, M.C., Jambor, J.L., Ptacek, C.J. and Blowes, D.W., 2009. Mine drainage from the
753 weathering of sulfide minerals and magnetite. Applied Geochemistry, 24(12): 2362-2373.

754 Moreau, J.W., Fournelle, J.H. and Banfield, J.F. 2013 Quantifying heavy metals sequestration by
755 sulfate-reducing bacteria in an acid mine drainage-contaminated natural wetland, Frontiers in
756 Microbiology, 4(43): 1-10.

757 Murowchick, J.B. and Barnes, H.L. 1986 Marcasite precipitation from hydrothermal solutions.
758 Geochimica et Cosmochimica Acta 50, 2615-2629.

759 Murphy, R. and Strongin, D.R., 2009. Surface reactivity of pyrite and related sulfides. Surface
760 Science Reports, 64(1): 1-45.

761 Nakashima, S. 1992 Complexation and reduction of uranium by lignite. Science of The Total
762 Environment 118, 425-437.

763 Nakashima, S., Disnar, J.R., Perruchot, A. and Trichet, J. 1984. Experimental-Study of Mechanisms
764 of Fixation and Reduction of Uranium by Sedimentary Organic-Matter Under Diagenetic or Hydrothermal
765 Conditions. Geochimica et Cosmochimica Acta 48, 2321-2329.

766 Nakashima, S., Disnar, J.R. and Perruchot, A. 1999. Precipitation kinetics of uranium by
767 sedimentary organic matter under diagenetic and hydrothermal conditions. Economic Geology and the
768 Bulletin of the Society of Economic Geologists 94, 993-1006.

769 Newsome, L., Morris, K. and Lloyd, J.R., 2014. The biogeochemistry and bioremediation of
770 uranium and other priority radionuclides. Chemical Geology, 363: 164-184.

771 Noël, V., Boye, K., Lezama Pacheco, J.S., Bone, S.E., Janot, N., Cardarelli, E., Williams, K.H. and
772 Bargar, J.R. 2017. Redox Controls over the Stability of U(IV) in Floodplains of the Upper Colorado River
773 Basin. Environmental Science & Technology 51, 10954-10964.

774 Nordstrom, D.K. and Southam, G. (Editors), 1997. Geomicrobiology of sulfide mineral oxidation.
775 Reviews in Mineralogy, 35. Mineralogical Sociaet of America, Washinton, 361-390 pp.

776 Och, L.M. and Shields-Zhou, G.A., 2012. The Neoproterozoic oxygenation event: Environmental
777 perturbations and biogeochemical cycling. Earth-Science Reviews, 110(1–4): 26-57.

778 Ohfuji, H. and Rickard, D., 2005. Experimental syntheses of framboids—a review. Earth-Science
779 Reviews, 71(3): 147-170.

780 O'Loughlin, E.J., Kelly, S.D., Cook, R.E., Csencsits, R. and Kemner, K.M. (2003) Reduction of
781 Uranium(VI) by Mixed Iron(II)/Iron(III) Hydroxide (Green Rust): Formation of UO2 Nanoparticles.
782 Environmental Science & Technology, 37: 721-727.

783 Qafoku, N.P., Kukkadapu, R.K., McKinley, J.P., Arey, B.W., Kelly, S.D., Wang, C., Resch, C.T.
784 and Long, P.E., 2009. Uranium in Framboidal Pyrite from a Naturally Bioreduced Alluvial Sediment.
785 Environmental Science & Technology, 43(22): 8528-8534.

786 Paterson, D., de Jonge, M.D., Howard, D.L., Lewis, W., McKinlay J., Starritt A., Küsel M., Ryan,
787 C.G., Kirkham, R., Moorhead, G., & Siddons, D.P. (2011) AIP Conf. Proc. 2011, 1365, 219−222.
788 http://scitation.aip.org/content/aip/proceeding/aipcp/10.1063/1.3625343

789 Percak-Dennett, E.M. and Roden, E.E. (2014) Geochemical and Microbiological Responses to
790 Oxidant Introduction into Reduced Subsurface Sediment from the Hanford 300 Area, Washington.
791 Environmental Science & Technology 48: 9197-9204.

792 Putnis, A., (2009) Mineral Replacement Reactions, Reviews in Mineralogy and Geochemistry, 70:
793 87-124.

794 Renshaw, J.C., Butchins, L.J.C., Livens, F.R., May, I., Charnock, J.M. and Lloyd, J.R. (2005)
795 Bioreduction of Uranium: Environmental Implications of a Pentavalent Intermediate. Environmental
796 Science & Technology 39, 5657-5660.

797 Rimstidt, J.D. Vaughan, D.J. 2003. Pyrite oxidation: A state-of-the-art assessment of the reaction
798 mechanism. Geochimica et Cosmochimica Acta 67(5):873-880. DOI: 10.1016/S0016-7037(02)01165-1

799 Regenspurg, S., Margot-Roquier, C., Harfouche, M., Froidevaux, P., Steinmann, P., Junier, P. and
800 Bernier-Latmani, R., 2010. Speciation of naturally-accumulated uranium in an organic-rich soil of an alpine
801 region (Switzerland). Geochimica et Cosmochimica Acta, 74(7): 2082-2098.

802 Renard, D. and Beucher, H., 2012. 3D representations of a uranium roll-front deposit. Applied
803 Earth Science, 121(2): 84-88.

804 Reynolds, R.L. and Goldhaber, M.B., 1983. Iron disulfide minerals and the genesis of roll-type
805 uranium deposits. Economic Geology, 78(1): 105-120.

806 Roberts, H.E., Morris, K., Law, G.T.W., Mosselmans, J.F.W., Bots, P., Kvashnina, K. and Shaw,
807 S. (2017) Uranium(V) incorporation mechanisms and stability in Fe(II)/Fe(III) (oxyhydr)oxide.
808 Environmental Science and Technology Letters, 4(10): 421-426.

809 Rosso, K.M. and Vaughan, D.J., 2006. Reactivity of Sulfide Mineral Surfaces. Reviews in
810 Mineralogy and Geochemistry, 61(1): 557-607.

811 Ryan, C., 2000. Quantitative trace element imaging using PIXE and the nuclear microprobe.
812 International Journal of Imaging Systems and Technology, 11(4): 219-230.

813 Ryan, C. and Jamieson, D., 1993. Dynamic analysis: on-line quantitative PIXE microanalysis and
814 its use in overlap-resolved elemental mapping. Nuclear Instruments and Methods in Physics Research
815 Section B: Beam Interactions with Materials and Atoms, 77(1): 203-214.

816 Ryan, C.G., Siddons, D.P., Kirkham, R., Li, Z.Y., Jonge, M.D.d., Paterson, D.J., Kuczewski, A.,
817 Howard, D.L., Dunn, P.A., Falkenberg, G., Boesenberg, U., Geronimo, G.D., Fisher, L.A., Halfpenny, A.,
818 Lintern, M.J., Lombi, E., Dyl, K.A., Jensen, M., Moorhead, G.F., Cleverley, J.S., Hough, R.M., Godel, B.,
819 Barnes, S.J., James, S.A., Spiers, K.M., Alfeld, M., Wellenreuther, G., Vukmanovic, Z. and Borg, S., 2014.
820 Maia X-ray fluorescence imaging: Capturing detail in complex natural samples. Journal of Physics:
821 Conference Series, 499(1): 012002.

822 Sachs, S., Reich, T. and Bernhard, G. (2010) Study of the role of sulfur functionalities in humic
823 acids for uranium(VI) complexation. Radiochimica Acta 98: 467-477.

824 Schoonen, M.A.A., 2004. Mechanisms of sedimentary pyrite formation. In: J.P. Amend, K.J.
825 Edwards and T.W. Lyons (Editors), Sulfur Biogeochemistry - Past and Present. Geological Society of
826 America.

827 Scott, T.B., Riba Tort, O. and Allen, G.C. (2007) Aqueous uptake of uranium onto pyrite surfaces;
828 reactivity of fresh versus weathered material. Geochimica et Cosmochimica Acta 71: 5044-5053.

829 Sharp, J.O., Lezama-Pacheco, J.S., Schofield, E.J., Junier, P., Ulrich, K.-U., Chinni, S., Veeramani,
830 H., Margot-Roquier, C., Webb, S.M., Tebo, B.M., Giammar, D.E., Bargar, J.R. and Bernier-Latmani, R.,
831 2011. Uranium speciation and stability after reductive immobilization in aquifer sediments. Geochimica et
832 Cosmochimica Acta, 75(21): 6497-6510.

833 Southam, G. and Saunders, J.A. (2005) The Geomicrobiology of Ore Deposits. Economic
834 Geology 100, 1067-1084.

835 Suzuki, Y., Kelly, S.D., Kemner, K.M. and Banfield, J.F., 2002. Radionuclide contamination:
836 Nanometre-size products of uranium bioreduction. Nature, 419(6903): 134-134.

837 Townsend, L.T., Shaw, S., Ofili, N.E.R., Kaltsoyannis, N, Walton, A.S., Mosselmans, J.F.W., Neill,
838 T.S., Lloyd J.R., Heath, S., Hibberd, R., Morris., K. (2020) Formation of U(VI)-persulfide Complex during
839 Environmentally relevant Sulfidation of Iron (oxyhy)droxides. Environmental Science & Technology 54
840 (1), 129-136.

841 Vimy, 2016. Significant Resource Upgrade for Mulga Rock Project. Vimy Resources Limited;
842 Annual Report 2016, p. 98. Perth.

843 Wang, Y., Frutschi, M., Suvorova, E., Phrommavanh, V., Descostes, M., Osman, A.A.A., Geipel,
844 G. and Bernier-Latmani, R. 2013a. Mobile uranium(IV)-bearing colloids in a mining-impacted wetland.
845 Nat Commun 4.

846 Wang, Z., Lee, S.-W., Kapoor, P., Tebo, B.M. and Giammar, D.E., 2013b. Uraninite oxidation and
847 dissolution induced by manganese oxide: A redox reaction between two insoluble minerals. Geochimica
848 et Cosmochimica Acta, 100: 24-40.

849 Wersin, P., Hochella Jr, M.F., Persson, P., Redden, G., Leckie, J.O. and Harris, D.W., 1994.
850 Interaction between aqueous uranium (VI) and sulfide minerals: Spectroscopic evidence for sorption and
851 reduction. Geochimica et Cosmochimica Acta, 58(13): 2829-2843.

852 Wilkin, R.T. and Barnes, H.L., 1997. Formation processes of framboidal pyrite. Geochimica et
853 Cosmochimica Acta, 61(2): 323-339.

854 Wilkin, R.T., Barnes, H.L. and Brantley, S.L., 1996. The size distribution of framboidal pyrite in
855 modern sediments: An indicator of redox conditions. Geochimica et Cosmochimica Acta, 60(20): 3897-
856 3912.

857 Wülser, P.-A., Brugger, J., Foden, J. and Pfeifer, H.-R., 2011. The Sandstone-Hosted Beverley
858 Uranium Deposit, Lake Frome Basin, South Australia: Mineralogy, Geochemistry, and a Time-Constrained
859 Model for Its Genesis. Economic Geology, 106(5): 835-867.

860 Yang, Z., Kang, M., Ma, B., Xie, J., Chen, F., Charlet, L. and Liu, C. (2014) Inhibition of U(VI)
861 Reduction by Synthetic and Natural Pyrite. Environmental Science & Technology 48, 10716-10724.

862 Zhang, Y., Lv, J., Dong, X, Fang, Q., Tan, W., Wu, X., Deng, Q (2020) Influence on Uranium (VI)
863 migration in soil by iron and manganese salts of humic acid: Mechanism and Behavior. Environmental
864 Pollution 256, 113369

865

866

Figure captions

Figure 1 Top, Map showing location of Mulga Rock near Kalgoorlie, Western Australia. Note that lakes shown are ephemial and/or salt, and the area is largely desert.

Bottom map shows the geological depiction and location of the Ambassador Deposit and borehole location of CD 1577 (UTM 51J: Easting 579942.81 mE, Northing 6682708.94 mS, depth = 43.5m) also shown are neighbouring Princess, Emperor and Shogun Deposits. Modified from Cumberland et al. (2018a) and from Vimy Resources (2016) report.

Figure 2 Details of the drilled core (CD1577). The sample analysed in this study formed part of the black peaty layer (37–44 m). The figure is adapted from the original core log (source Vimy archives). Note the gamma spectra on the right are shown on a log scale.

Figure 3 (A) False colour red–green–blue XFM map of pyrite grain 1, red = Fe, green = U and blue = S, showing pyrite surrounded by U. (B) False colour red–green–blue XFM map of pyrite grain 2, red = S, green = U and blue = Fe, showing pyrite surrounded by U. The very dark regular shapes at the top right and left of the pyrite grain contain Si. The rectangles indicate the approximate region of the transects used for the μXANES analysis.

Figure 4 General area detector diffraction system (GADS) generated μXRD pattern with reference peaks. The main phase is pyrite (blue) (Bayliss, 1977) with traces of millerite (pink) (RRUFF-ID-R060898, Orford, Quebec, Canada) and marcasite (light blue) (RRUFF-ID-R060882, Racine, Wisconsin, USA). X-ray beam source was a Cu Kα, 800 μm focussed beam.

Figure 5(A) Back scattered SEM–EDX elemental map of a pyrite grain within the lignite sample. (B) relative abundances of elements (wt. %). (c) C, Fe, O, S, Si, S, U maps. A correlation analysis of these maps is available in the supporting information (Figures S3 and S4). The sample was preserved by C-bearing resin impregnation, so the map of C should be interpreted with caution. All scale bars represent 100 μm.

Figure 6 High resolution SEM images of framboidal-like pyrite crystal grains from pyrite grain 1. (A) Pyrite–U boundary; (B) and (C) show the centre of the framboidal-like pyrite. The square in B indicates the site of EDX analysis. (D) Enlargement of the rectangle shown in C. Lower contrast phases in C and D are mostly Fe and S and the brightest phases, is a mixed phase containing U, Fe, S and O.

39

Figure 7 (A) General area detector diffraction system (GADS) μXRD patterns for a transect across a pyrite grain edge. Analysis was performed using a Cu Kα 300 μm focussed beam (smallest resolvable beam size); (B) Pattern for pyrite-rich area (a, blue) with corresponding reference peaks for pyrite (Bayliss, 1977); and (C) Pattern for U-rich area (b, green), with corresponding reference peaks for coffinite (Fuchs and Gilbert 1958).

Figure 8 Distribution and concentration of Fe, S, U, and U oxidation state on a transect across pyrite grain 1. (A–D) XFM element maps; scales are in microns and concentration in wt.%. (A) Composite Red Green Blue (Fe, S and U); (B) Fe map; (C) S map; (D) U map. Rectangles show the segments from which the U spectra were extracted. (E) Bar chart showing U(IV):U(VI) ratios derived from U L_3 μXANES spectra for the boxes shown in (D). (F) Element concentrations of Fe (red) and U (green) on the same transect. The S concentration is semi-quantitative (see text for details).

Figure 9 Distribution and concentration of Fe, S, U, and U oxidation state on a transect of 'pyrite grain 2'. (A–D) XFM element maps; scales are in microns and concentration in wt.%. (A) Composite Red Green Blue (Fe, S and U); (B) Fe map; (C) S map; (D) U map. Rectangles show the segments from which the U spectra were extracted. (E) Bar chart showing U(IV):U(VI) ratios derived from U L_3 μXANES spectra for the boxes shown in (D); (F) Element concentrations of Fe (red) and U (green) on the same transect. The S concentration is semi-quantitative (see text for details).

Table captions

Table 1 Results of linear combination fitting for uranopilite and coffinite (tests 1, 3), and uranopilite and uraninite (tests 2, 4) for pyrite grains 1 and 2. Values represent the proportion of U present in the specified oxidation state.

40

926 Figure 1

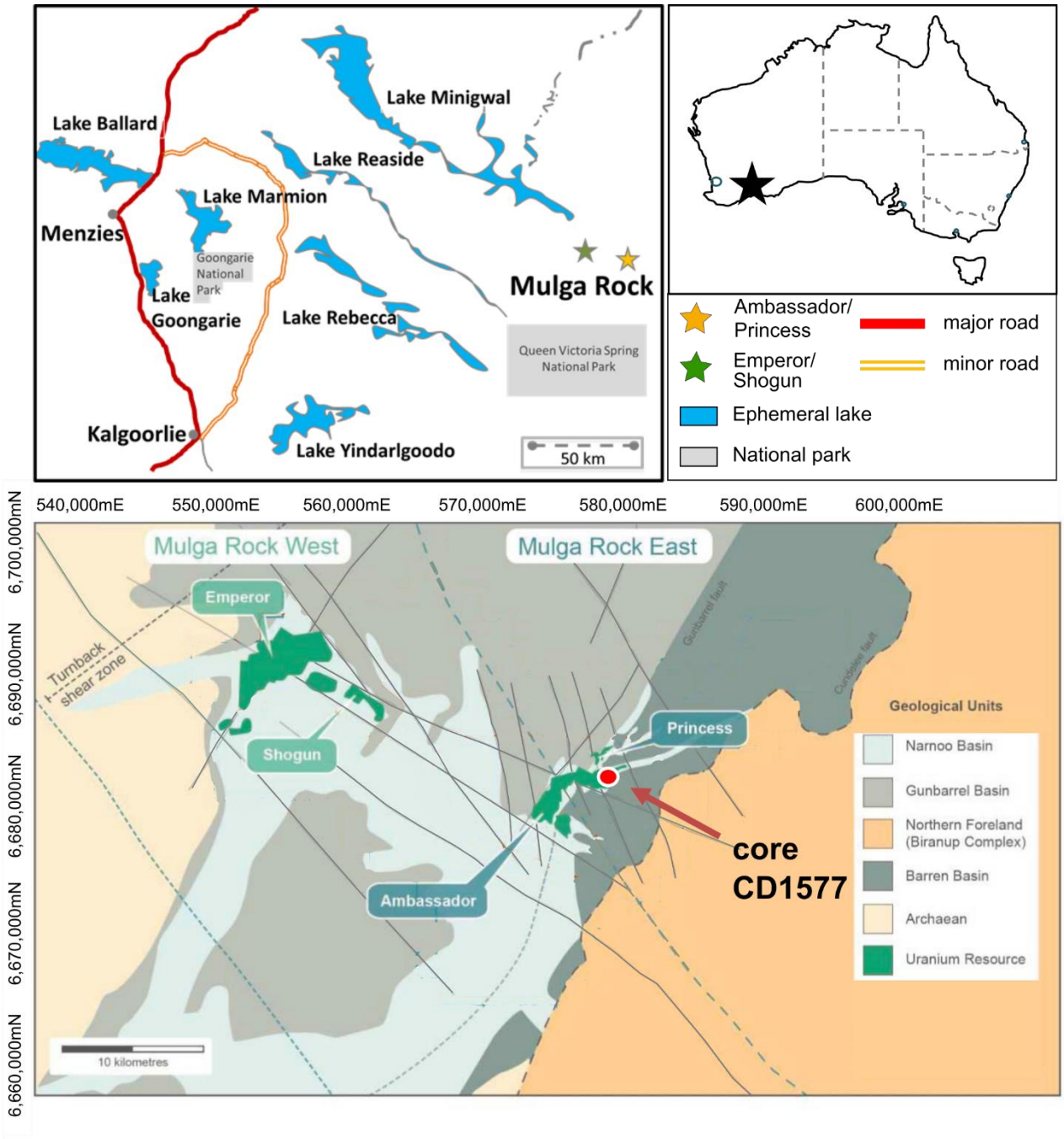

927

928

41

929 Figure 2

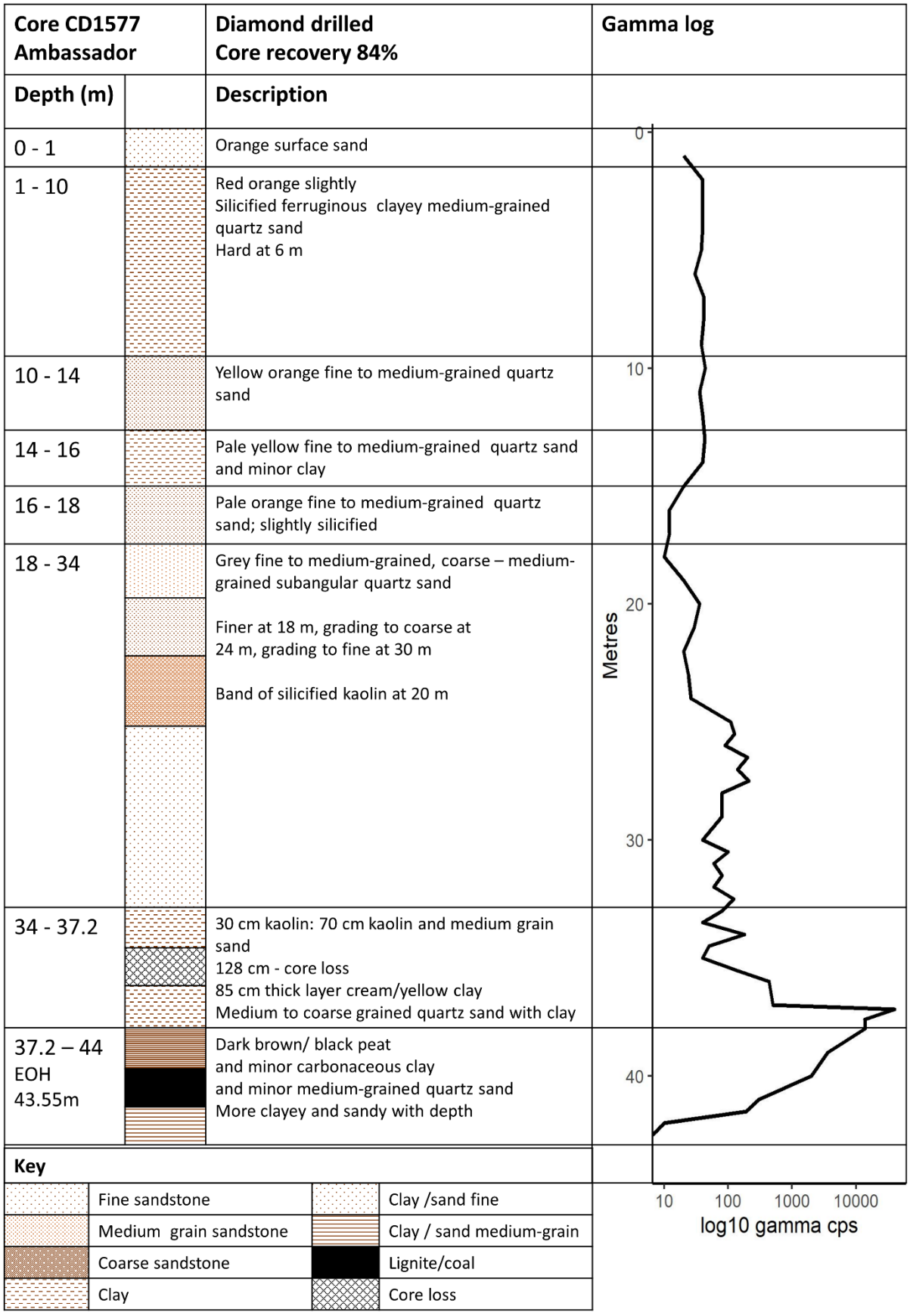

930

42

931 Figure 3

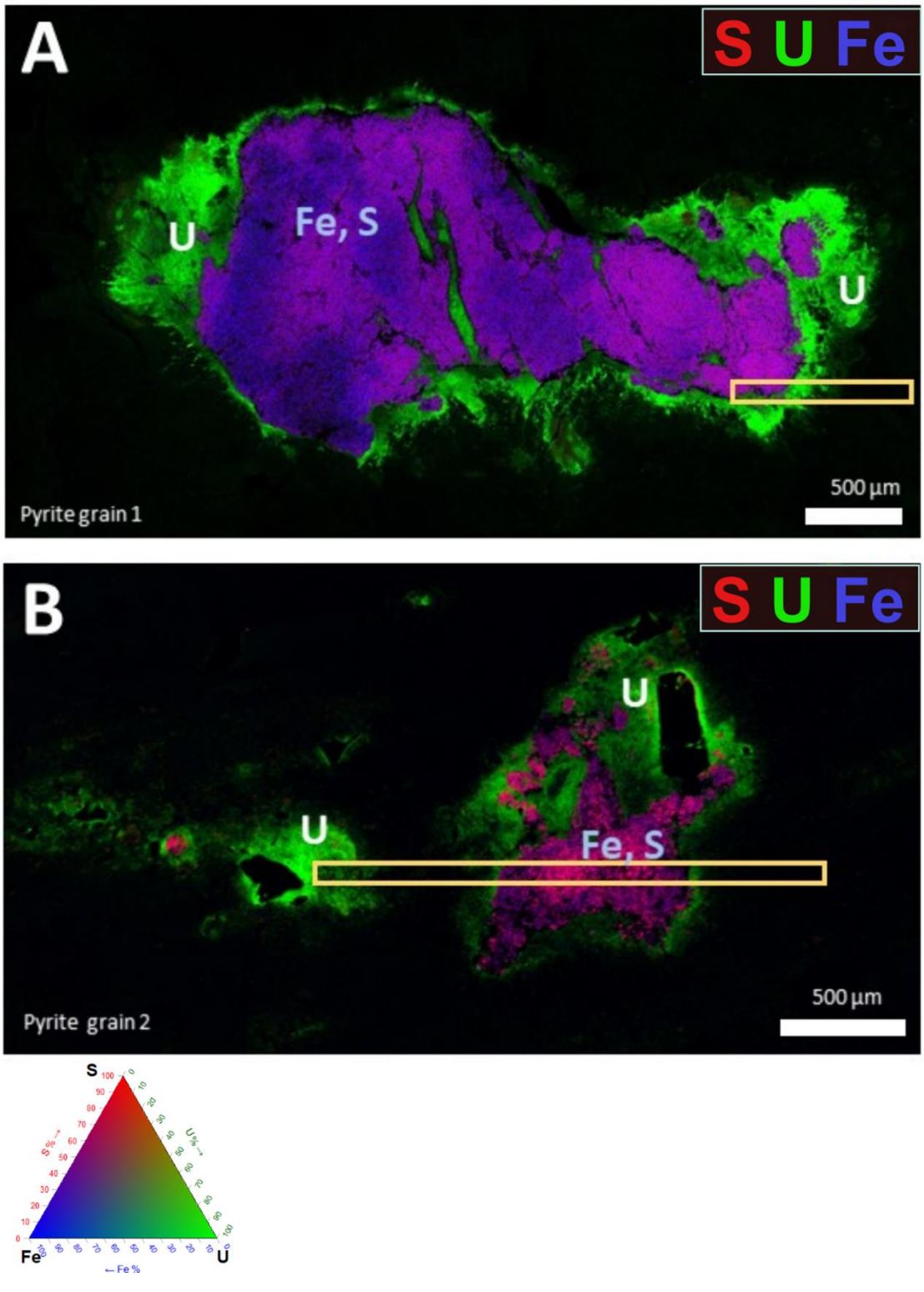

932

933

43

934 Figure 4

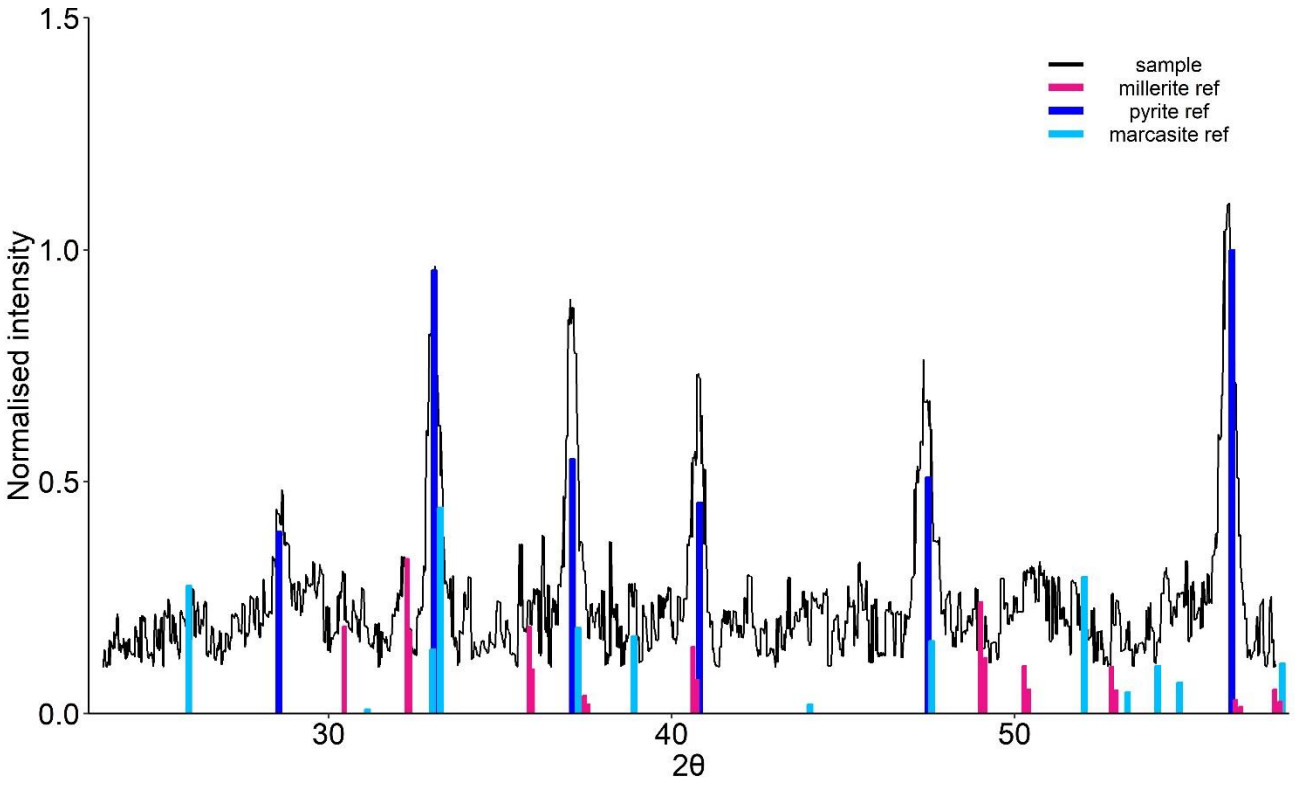

935

936

44

937 Figure 5

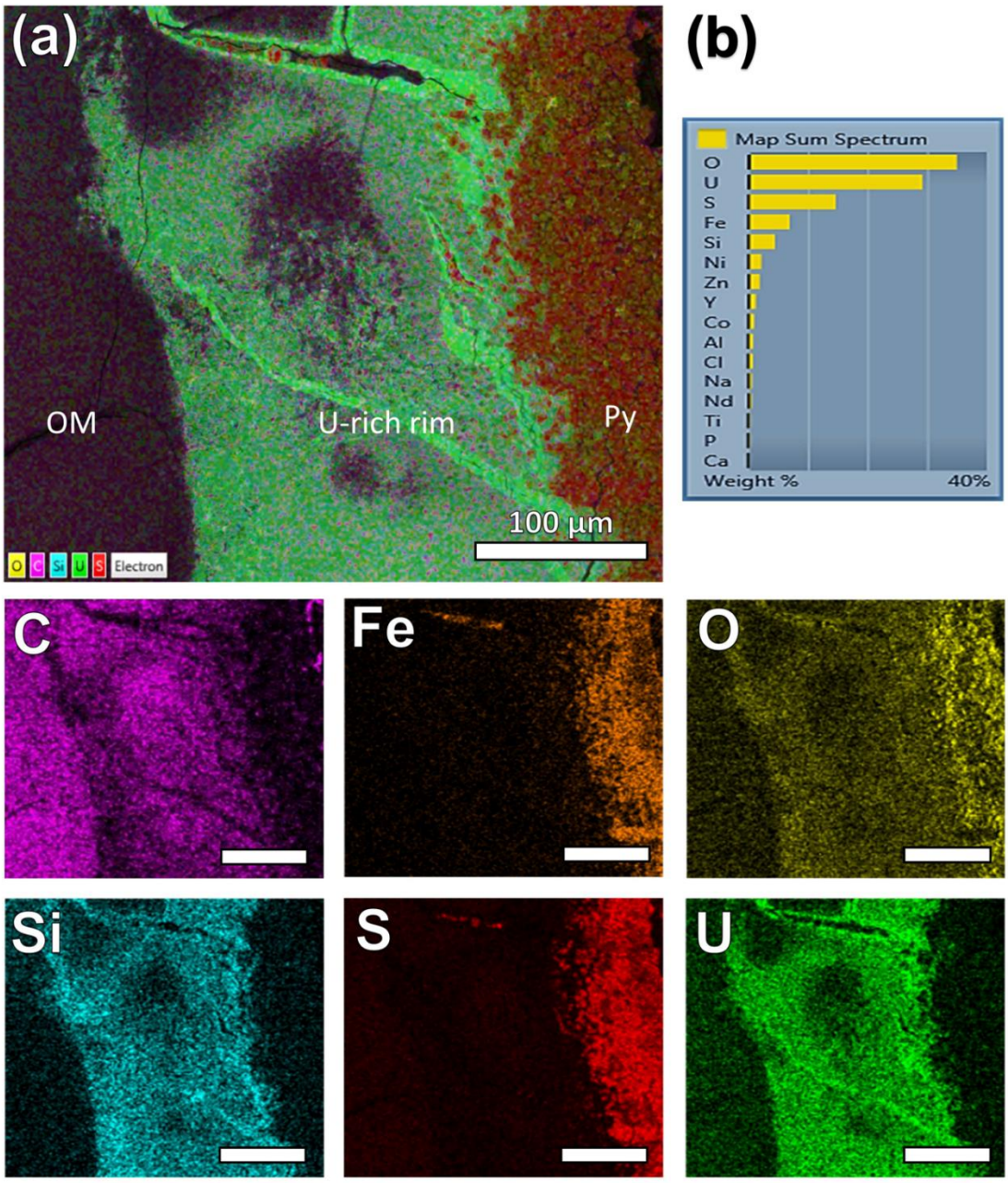

938

939

45

940 Figure 6

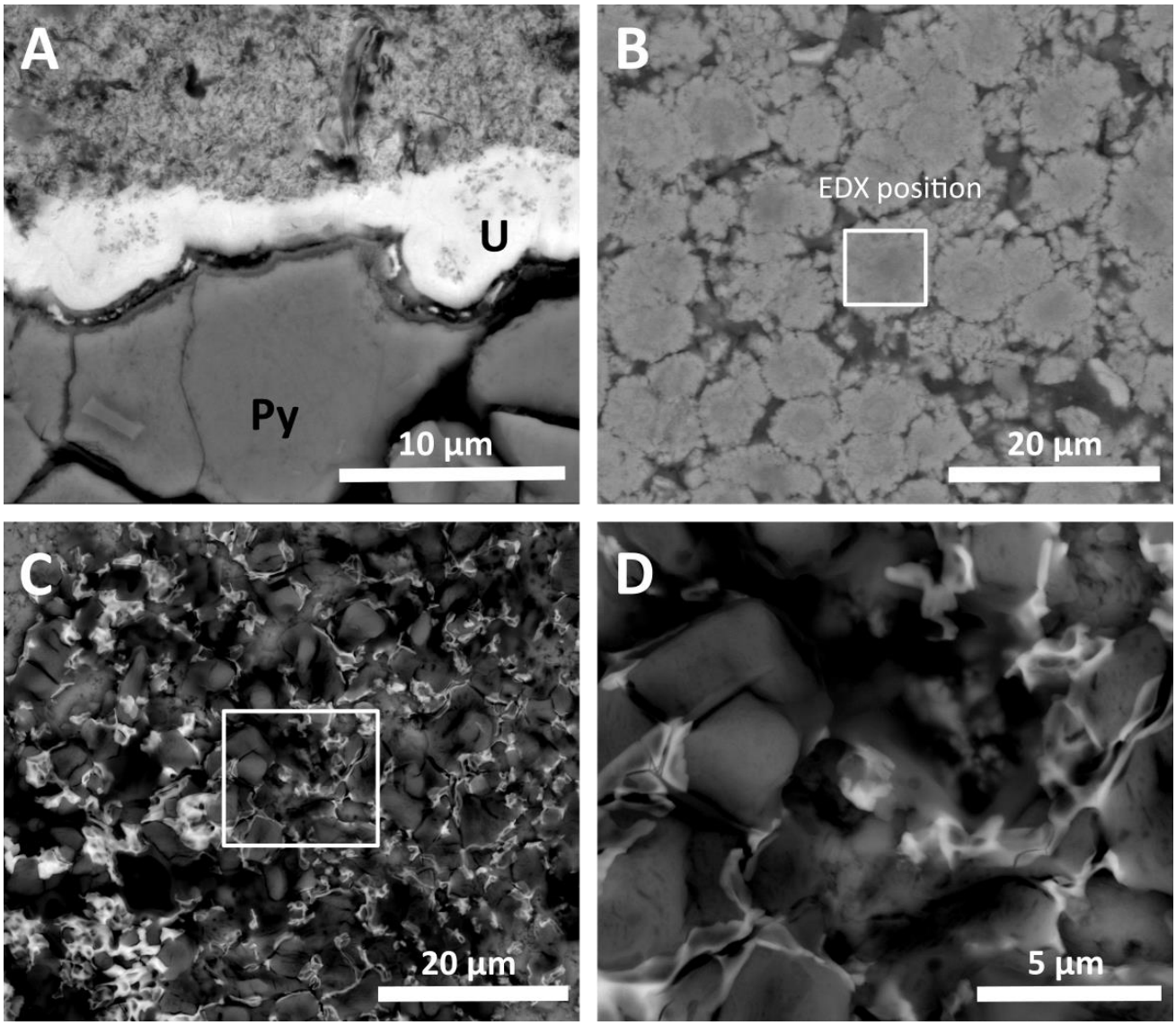

941

942

46

943 Figure 7

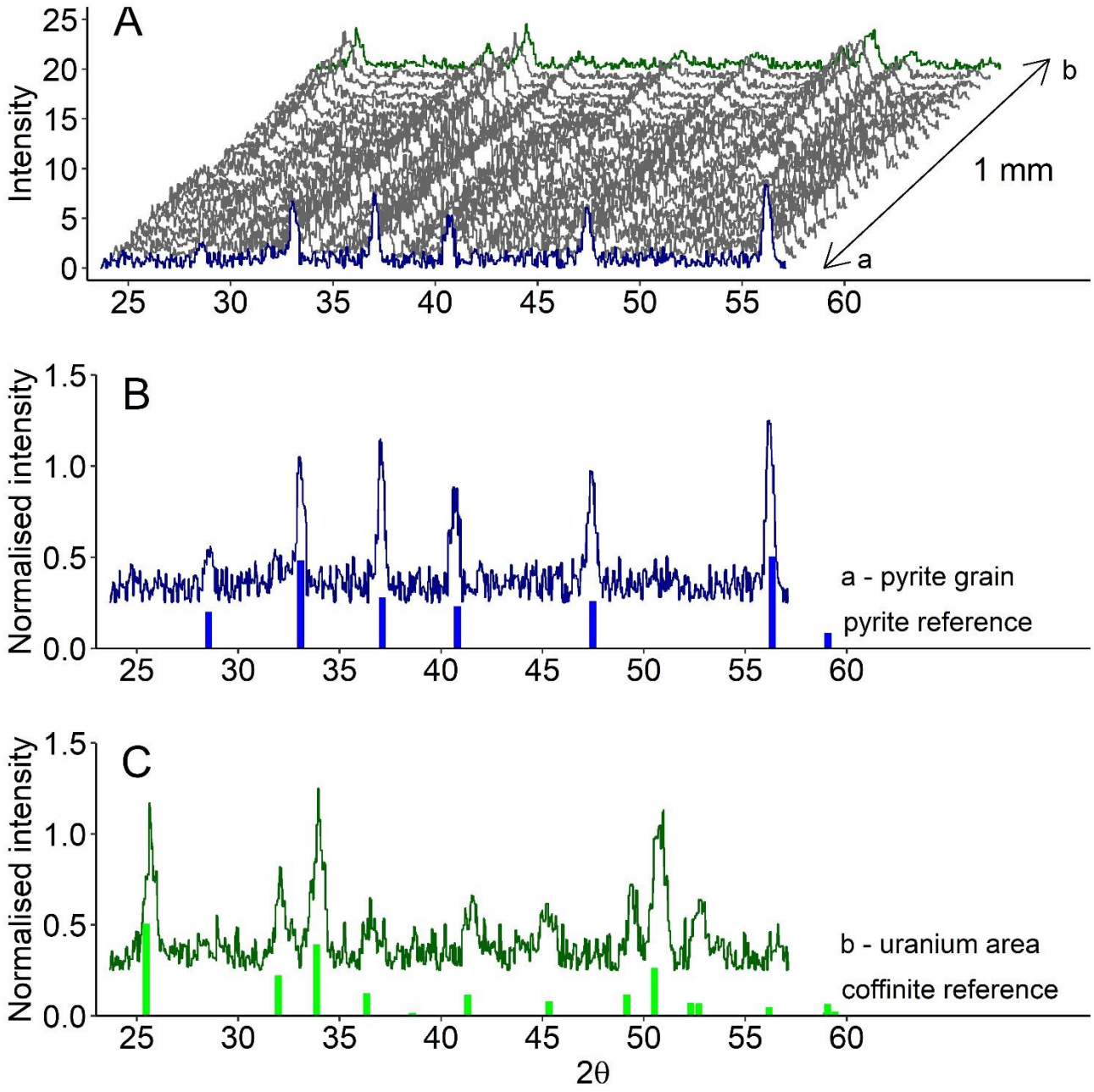

944

945

47

946 Figure 8

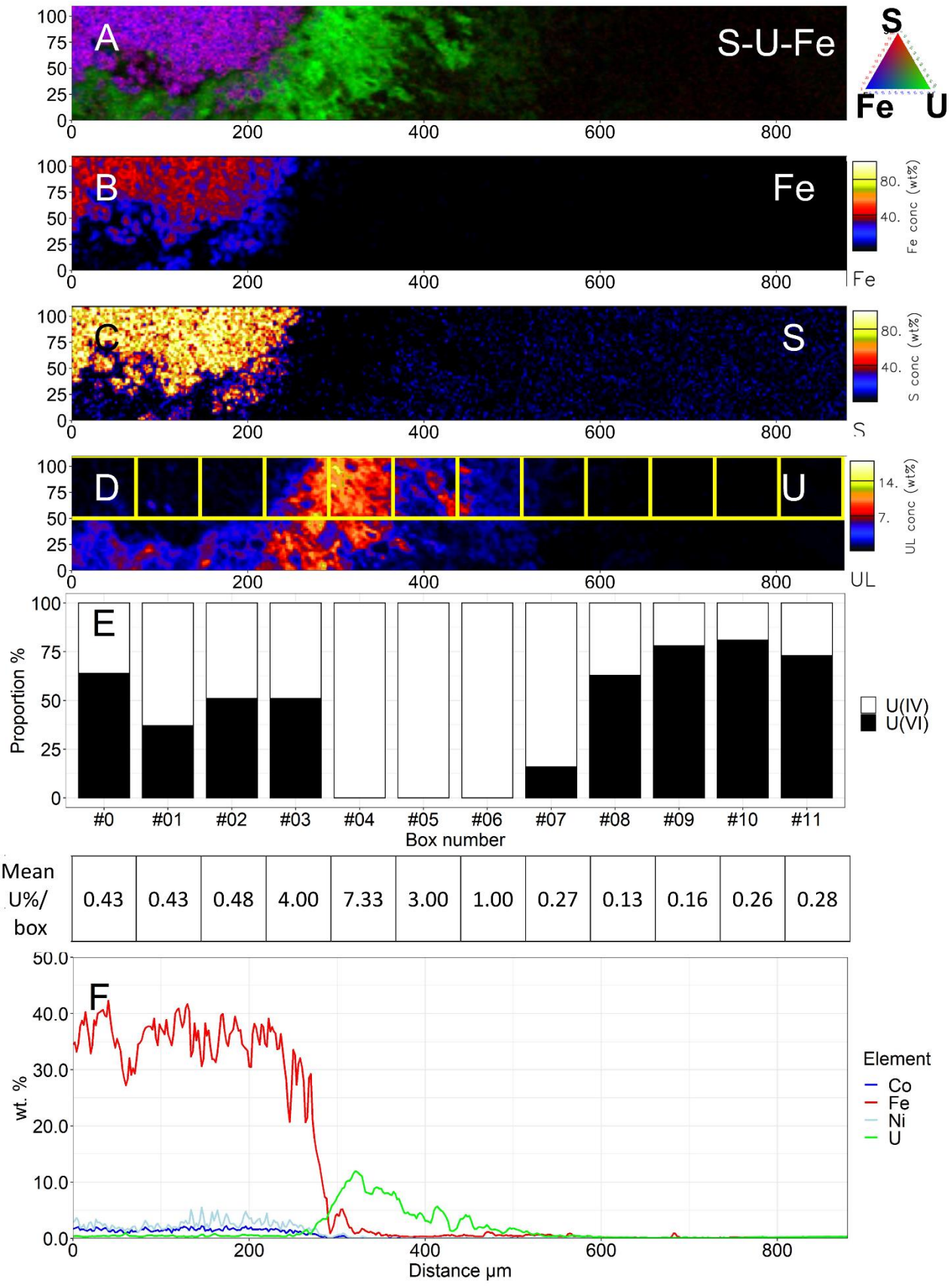

947

48

948 Figure 9

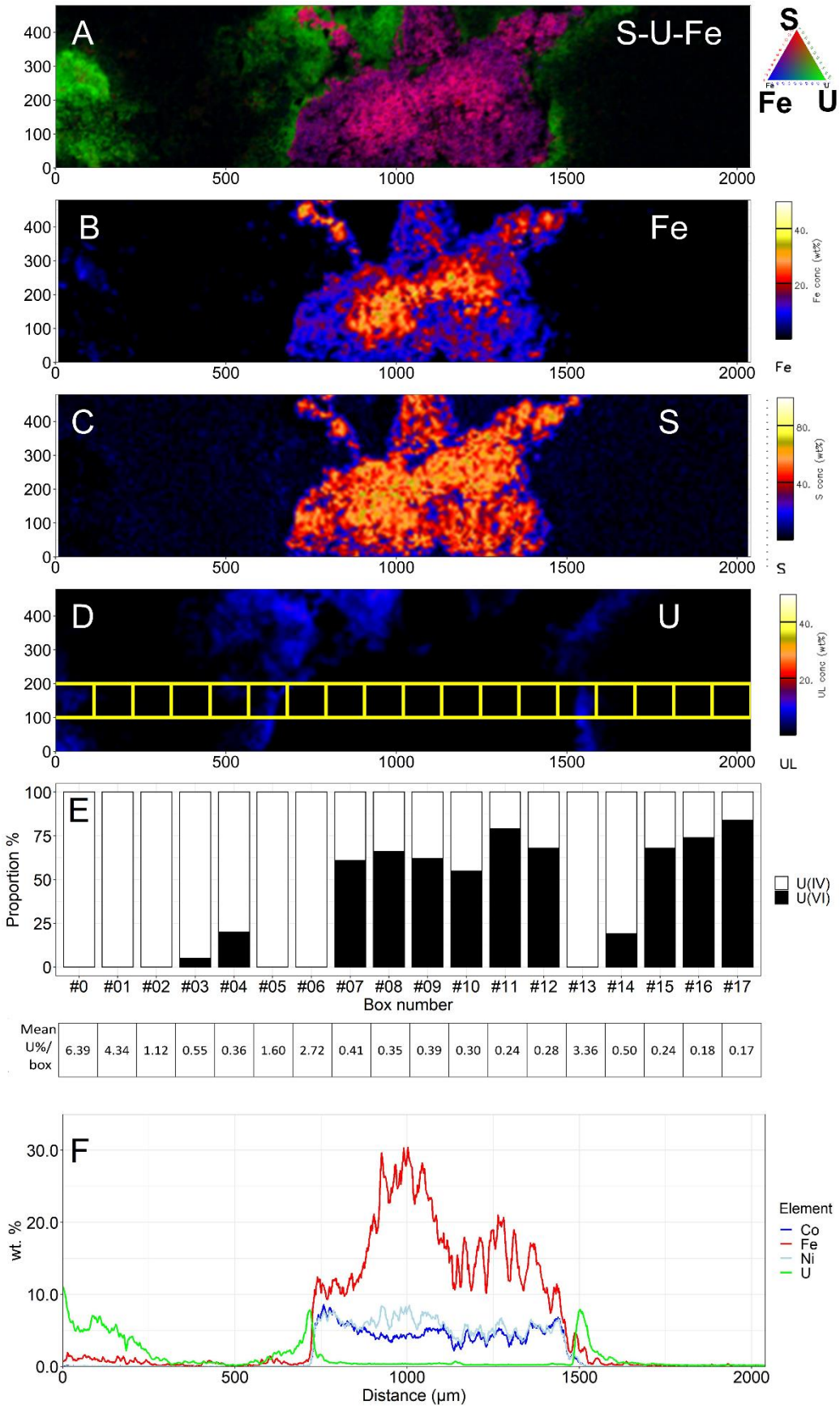

949

49

950 **Table 1**

951

μXANES Transect segment number	LCF TEST 1 urano-pilite weight	coffinite weight	uranopilite error ±	coffinite error ±	R-factor	LCF TEST 2 urano-pilite weight	uraninite weight	uranopilite error ±	uraninite error ±	R-factor
#0	0.65	0.35	0.13	0.05	0.007	0.59	0.41	0.15	0.09	0.010
#1	0.37	0.63	0.12	0.02	0.001	0.29	0.71	0.15	0.10	0.011
#2	0.51	0.49	0.12	0.03	0.002	0.45	0.55	0.14	0.08	0.008
#3	0.51	0.49	0.12	0.03	0.002	0.45	0.55	0.14	0.08	0.008
#4	0.00	1.00	0.12	0.00	0.008	0.00	1.00	0.12	0.00	0.046
#5	0.00	1.00	0.12	0.00	0.004	0.00	1.00	0.12	0.00	0.034
#6	0.00	1.00	0.12	0.00	0.007	0.00	1.00	0.12	0.00	0.041
#7	0.16	0.84	0.12	0.04	0.004	0.05	0.95	0.19	0.14	0.023
#8	0.64	0.36	0.16	0.11	0.030	0.56	0.44	0.20	0.16	0.033
#9	0.79	0.21	0.14	0.08	0.019	0.74	0.26	0.17	0.13	0.020
#10	0.82	0.18	0.14	0.07	0.014	0.76	0.24	0.16	0.11	0.015
#11	0.73	0.27	0.13	0.05	0.006	0.67	0.33	0.14	0.08	0.007
mean	*0.43*	*0.57*	*0.13*	*0.04*	*0.01*	*0.38*	*0.62*	*0.15*	*0.08*	*0.02*
SD	*0.32*	*0.32*	*0.01*	*0.03*	*0.01*	*0.30*	*0.30*	*0.03*	*0.06*	*0.01*

μXANES Transect segment number	LCF TEST 3 urano-pilite weight	coffinite weight	uranopilite error ±	coffinite error ±	R-factor	LCF TEST 4 urano-pilite weight	uraninite weight	uranopilite error ±	uraninite error ±	R-factor
#0	0.00	1.00	0.12	0.00	0.040	0.00	1.00	0.00	0.00	0.040
#1	0.00	1.00	0.12	0.00	0.039	0.00	1.00	0.00	0.00	0.039
#2	0.00	1.00	0.12	0.00	0.030	0.00	1.00	0.00	0.00	0.030
#3	0.05	0.95	0.12	0.03	0.024	0.00	1.00	0.00	0.03	0.024
#4	0.21	0.79	0.13	0.05	0.022	0.08	0.92	0.14	0.05	0.022
#5	0.00	1.00	0.12	0.00	0.036	0.00	1.00	0.00	0.00	0.036
#6	0.00	1.00	0.12	0.00	0.041	0.00	1.00	0.00	0.00	0.041
#7	0.61	0.39	0.12	0.04	0.008	0.55	0.45	0.08	0.04	0.008
#8	0.67	0.33	0.13	0.05	0.010	0.63	0.37	0.09	0.05	0.010
#9	0.62	0.38	0.12	0.03	0.007	0.56	0.44	0.07	0.03	0.007
#10	0.55	0.45	0.12	0.04	0.009	0.51	0.49	0.09	0.04	0.009
#11	0.80	0.20	0.15	0.09	0.021	0.76	0.24	0.13	0.09	0.021
#12	0.69	0.31	0.13	0.06	0.013	0.65	0.35	0.10	0.06	0.013
#13	0.00	1.00	0.12	0.00	0.048	0.00	1.00	0.00	0.00	0.048
#14	0.19	0.81	0.12	0.03	0.019	0.06	0.94	0.13	0.03	0.019
mean	*0.29*	*0.71*	*0.12*	*0.03*	*0.02*	*0.25*	*0.75*	*0.06*	*0.03*	*0.02*
SD	*0.32*	*0.32*	*0.01*	*0.03*	*0.01*	*0.31*	*0.31*	*0.06*	*0.03*	*0.01*

952